Journal of Nuclear Materials 447 (2014) 125–142

Contents lists available at ScienceDirect

Journal of Nuclear Materials

journal homepage: www.elsevier.com/locate/jnucmat

Thermo-mechanical analysis of LWR SiC/SiC composite cladding ☆

M. Ben-Belgacem [a,1], V. Richet [a,1], K.A. Terrani [b,*], Y. Katoh [b], L.L. Snead [b]

[a] École Polytechnique, Palaiseau Cedex 91128, France
[b] Oak Ridge National Laboratory, Oak Ridge, TN 37831, USA

ARTICLE INFO

Article history:
Received 13 September 2013
Accepted 2 January 2014
Available online 9 January 2014

ABSTRACT

A dedicated framework for thermo-mechanical analysis of the in-pile performance of SiC/SiC composite fuel cladding concepts in LWRs has been developed. This analysis framework focuses on cladding and omits any fuel-cladding interaction and fuel behavior. Since radial expansion of the cladding occurs early in life for these ceramic structures, fuel-cladding contact is expected to be delayed or eliminated and therefore it is not considered in this analysis. The analysis inputs recent out-of-pile and in-pile materials property data and phenomenological understanding of material evolution under neutron irradiation for nuclear-grade SiC/SiC composites to provide a best-estimate analysis. The analysis provides insight into the concept design and feasibility of SiC/SiC composite cladding concepts that exhibit significantly different behavior than metallic cladding structures. In particular, absence of any tangible creep (thermal or irradiation) coupled with a large and temperature-gradient-driven irradiation swelling strain gradient across the cladding, drive development of large stresses across the cladding thickness. The resulting analysis indicates that significant stresses develop after a modest neutron dose (~1 dpa) and a pronounced variation across the cladding thickness exists and is opposite to that observed for metallic cladding structures where swelling or growth strains are either negligible (with small temperature dependence) or absent. Following this thermo-mechanical analysis, a best-estimate and parametric examination of SiC/SiC fuel rod cladding structures has been performed using appropriate Weibull statistics to prescribe basic design guidelines and to begin to define a probable design space.

1. Introduction

Application of silicon carbide (SiC) in nuclear systems dates back to the 1960s as nuclear fuel constituents for high-temperature gas reactors [1,2]. Since that time, SiC materials have been examined extensively as fuel and structural materials in fission and fusion systems [3,4], though up to this point have still not found application outside the original nuclear fuel form. While structural applications of SiC have been discussed since the early days of fusion reactors [5], serious discussion and development were not considered until well after the invention of the continuous SiC-based Nicalon fiber [6]. This continuous fiber, the so-called Nicalon™ SiC fiber, could be fabricated in tow form and textile woven, allowing composites of chemically vapor infiltrated (CVI) SiC to be formed. Through the late 1980s and 1990s the aerospace, fossil energy, and fusion communities pursued development programs producing and testing myriad composites for thermo-structural applications [7].

In many ways the development paths in the non-nuclear and nuclear (fusion) programs over the early decades of SiC composite development shared similar goals. Early studies recognized the merits of continuous-fiber over whisker or platelet composite forms to maximize toughness, and the critical need for and optimization of the fiber/matrix interphase were studied in detail. For both high-temperature and irradiation performance, the ceramic-grade Nicalon™ fibers were found to be unstable, due to the presence of a large siliconoxycarbide phase (>20%). This led to the development of fibers of successively higher purity and crystallinity such as the current Nicalon Type-S and the Tyranno SA. Issues related to the poor performance of non-stoichiometric fibers and forms of SiC and the importance of the fiber matrix interface can be found elsewhere [8]. For purposes of this discussion [for the temperatures, doses, and assumed application stress conditions of a light water reactor (LWR) fuel clad application], it is sufficient to state that currently only two matrix and two fiber systems are known to be stable: CVI SiC and nano-powder SiC based (so-called NITE) matrices and Nicalon Type-S and Tyranno SA fibers.

Outside the nuclear community, SiC/SiC composites have gained commercial traction for niche applications, especially for

☆ The United States Government retains, and by accepting the article for publication, the publisher acknowledges that the United States Government retains, a nonexclusive, paid-up, irrevocable, worldwide license to publish or reproduce the published form of this work, or allow others to do so, for United States Government purposes.

* Corresponding author. Tel.: +1 865 576 0264.
E-mail address: terranika@ornl.gov (K.A. Terrani).
1 Student assignee at Oak Ridge National Laboratory.

0022-3115/$ - see front matter © 2014 Elsevier B.V. All rights reserved.
http://dx.doi.org/10.1016/j.jnucmat.2014.01.006

Nomenclature

k	thermal conductivity (W/m K)	P_e	exterior pressure (Pa)
R	thermal resistivity (m K/W)	P_i	interior pressure (Pa)
ρ	mass density (kg/m^3)	E	Young's modulus (1D model) (Pa)
α	coefficient of thermal expansion (K^{-1})	ν	Poisson's ratio (1D model) (Pa)
C_p	specific heat capacity (J/kg K)	$\sigma_r, \sigma_\theta, \sigma_z$	radial, azimuthal and axial stress (1D model) (Pa)
T	temperature (K)	$\varepsilon_r, \varepsilon_\theta, \varepsilon_z$	radial, azimuthal and axial strain (1D model)
q	heat flux (W/m^2)	E_p, E_r	in-plane and through-thickness Young's modulus (2D model) (Pa)
S	swelling	ν_p, ν_r	in plane and through thickness Poisson's ratio (2D model)
h	heat transfer coefficient (W/m^2 K)	G	through thickness shear modulus (Pa)
T_c	coolant temperature (K)	$\sigma_{rr}, \sigma_{\theta\theta}, \sigma_{zz}, \sigma_{zr}$	radial, azimuthal, axial, and shear stress (2D model) (Pa)
r_i	interior radius	$\varepsilon_{rr}, \varepsilon_{\theta\theta}, \varepsilon_{zz}, \varepsilon_{zr}$	radial, azimuthal, axial, and shear strain (2D model)
r_e	exterior radius		
$\dot{\varepsilon}^c$	creep strain rate (s^{-1})		
L	clad length		
D	dose (dpa)		
dt	time increment (s)		
$\triangle r$	spatial increment (m)		

high-temperature hostile environments. Examples include combustor liners and first-stage shrouds of industrial gas turbines as well as engine components in GE military and commercial aircraft engines [9]. To date there have been no adoptions or prototype applications of SiC in commercial or test reactors, though they have been in the design phase for specialty load-carrying components in high-temperature gas-cooled reactors, and now boiling water reactor (BWR) fuel assembly channelboxes are being mocked up and tested [10,11].

Since the Three Mile Island accident, another LWR application of SiC has been discussed and developed through a number of privately and government funded avenues. Specifically, a continuous-fiber composite, over-coated with thick chemically vapor deposited (CVD) SiC, is under consideration for Zr alloy cladding replacement [12–14]. While some of the benefits will be touched on in this paper, and have been outlined previously, the irradiation behavior of the underlying composite constituents are now well understood [4,8]. However, up to this point reporting on basic thermo-mechanical analyses that would underpin the concept and potentially the design of the component architecture has been sparse. Carpenter [15] initially examined the behavior of a PWR pin with a three-layer SiC cladding (monolith-composite-monolith) by modifying the FRAPCON fuel performance code [16] with SiC material property data. While some important observations were made during his analysis (i.e. radial expansion of the cladding and development of a large temperature gradient across the cladding early on in fuel lifetime), assumption of a constant swelling strain across the cladding thickness (essentially ignoring the temperature dependence of the swelling) led to miscalculation of the magnitude and shape of the principal stresses across the cladding. Another analysis sponsored by the Electric Power Research Institute (EPRI) and carried out with the FALCON fuel performance code [17], inputting similar material property data as the previous study, concluded that pellet-cladding contact occurs at high fuel burnups (~60–70 MWd/kg U) and can readily lead to failure of the cladding [18].

In this paper one-dimensional (1D) finite-difference and two-dimensional (2D) finite-element methodologies have been used to assess heat transfer and the mechanical response of SiC/SiC composite fuel cladding structures subjected to nominal LWR operating conditions. The analysis was focused on the cladding and no attempt was made to capture the behavior and evolution of the fuel pellet. The fuel or gap properties do not affect the heat flux flowing into the cladding and the value of this parameter can be fully captured by the rod operating power. In conventional fuel rods, the pellet experiences cracking shortly after reactor startup. Accordingly it relocates to become partially in contact with the cladding. However, this mode of contact does not exert any force on the cladding. Only after the magnitude of cladding creepdown and pellet swelling strains add up to the gap thickness a hard contact between the two resulting in force exertion on the cladding can be assumed. As it will be discussed later in the text, cladding creep down is absent in case of SiC cladding and instead radial expansion due to volumetric swelling expands the pellet-cladding gap. Accordingly, hard contact between the pellet and cladding inner wall can be neglected as discussed in Section 4.1. Also, a linear fission gas release rate from the fuel with respect to time is assumed that is very simplistic yet purposeful as discussed in Section 2.1.6. Unirradiated and dose-dependent material properties input to the models are from the latest and most pertinent experimental data available from high purity SiC fiber/CVI matrix composites [4,8]. The methodologies are described in detail in the text and the accompanying appendix to provide complete clarity and results from the 1D and 2D analyses are presented for multiple cases with a systematic parametric approach for the benefit of the reader. Finally, a discussion is offered that provides a context for the results and the implications for fuel operation.

2. Methodology

2.1. Material properties

To produce an accurate prediction of the thermo-mechanical behavior of SiC/SiC cladding structures under reactor operating conditions, an accurate set of unirradiated and dose-dependent material property data are necessary. In this section various material properties that are input to the analytical model are discussed.

2.1.1. Swelling

For discussion purposes, the primary fast-neutron irradiation-induced phenomenon to consider is swelling. This is the case since swelling is a measure of the extent of irradiation-induced defects that are present in the material. These same defects, or others with a proportional population, are considered responsible for the evolution of the various material properties, such as thermal conductivity, under irradiation [4]. Accordingly swelling provides a good basis for discussion of dose-dependent properties in the later sections. Given the basic assumption that macroscopic swelling, isotropic in nature in the absence of any deviatoric stress components, originates primarily from the buildup of Frenkel defects in the lattice in the temperature range of present interest, it is viable to proceed with a prediction of its magnitude as a function of temperature and dose using basic rate theory equations. This is indeed the approach demonstrated by Katoh et al. [8,19] to reproduce the experimental neutron and ion irradiation data in intermediate temperatures. Briefly, the approach considers vacancies immobile, and therefore the rate of vacancy population evolution is dictated by production proportional to dose rate and annihilation via recombination with migrating self-interstitial atoms (SIAs). Therefore, given an SIA population at any time, the vacancy concentration is readily determined. The SIAs are produced at the same rate as the vacancies; however, their annihilation in addition to bulk recombination takes place via diffusion to sinks. As supported by microscopic examinations, the dominant sinks in SiC under intermediate-temperature irradiations are SIA clusters/loops [4,20,21]. Taking into account the dose- and temperature-dependent size and population of these loops, the SIA and vacancy concentrations can be predicted at any given time. These mechanisms dictate a 2/3 dependence of vacancy concentration and thereby swelling on dose until a saturation is approached. As the loop density and size increase and the vacancy population builds up, the system reaches an equilibrium where the recombination rate equals that of production. This marks the onset of swelling saturation and is essentially the manifestation of the "irradiation induced irradiation resistance" mechanism dubbed previously by Katoh.

Once these basic principles are established, swelling can be accurately interpolated as a function of dose and temperature between the available neutron and ion irradiation data. Accordingly, the spatial dependence of swelling across the cladding thickness can be modeled. The logarithmic swelling may be expressed as a linear function of the temperature summed with a linear function of the logarithm of the dose. Consequently, the formula used for 2D interpolation of the available experimental data points is the following:

$$ln(S_n) = a_1 + b_1 T_n + c_1 ln(D), \quad (1)$$

where a_1, b_1 and c_1 are numerical fits to the available experimental data, D is the dose, and n is the index of the spatial element since temperature varies across the cladding height and thickness. The numerical fits are not global values and are evaluated by fitting the three sets of experimental data closest to the dose and temperature space of interest with Eq. (1). This approach enables accounting for saturation in swelling at high doses. Fig. 1 shows some of the experimental data points along with the extrapolated contour map of swelling as a function of temperature and dose.

2.1.2. Thermal conductivity

A large body of work is available on the effects of irradiation on thermal conductivity of ceramics [23,24,4]. Ignoring electronic thermal transport at high temperatures, the thermal conductivity of ceramics can be simply estimated as the inverse of the sum of thermal resistivities as follows:

$$\frac{1}{k} = R_m + R_{gb} + R_U + R_{id}, \quad (2)$$

where R stands for thermal resistivity and subscripts m, gb, U, and id designate matrix, grain boundary, Umklapp (phonon–phonon), and irradiation defect, respectively. Note that the matrix resistivity term takes into account the effect of defects present in the lattice in the unirradiated state. The temperature-dependent magnitude of the first three terms in Eq. (2) can be determined exactly by measuring the thermal conductivity of unirradiated material. In this study, the temperature-dependent magnitude of these terms is directly taken from experimental data for the SA3-PyC150A SiC/SiC composite reported in Ref. [8]. The magnitude of resistance due to irradiation defects depends on the type and density of defects in the lattice that form as a result of irradiation. As one can recall in the previous section, swelling was noted to be a fairly accurate measure of the concentration of irradiation-induced defects in SiC. Therefore all that is necessary for prediction of irradiation-induced defect resistivity is a proportionality factor between this term and the swelling. These proportionality factors have been measured following irradiation for both monolithic SiC and SiC/SiC composites and are reported in Ref. [4,8], respectively. Incorporation of these experimental data coupled with the swelling model described earlier into this simple methodology yields the temperature- and dose-dependent thermal conductivity values for SiC/SiC specimens in this study. Fig. 2 shows a map of thermal conductivity for SA3-PyC150A SiC/SiC composite as a function of irradiation dose and temperature. Note that this particular composite exhibits a high thermal conductivity when

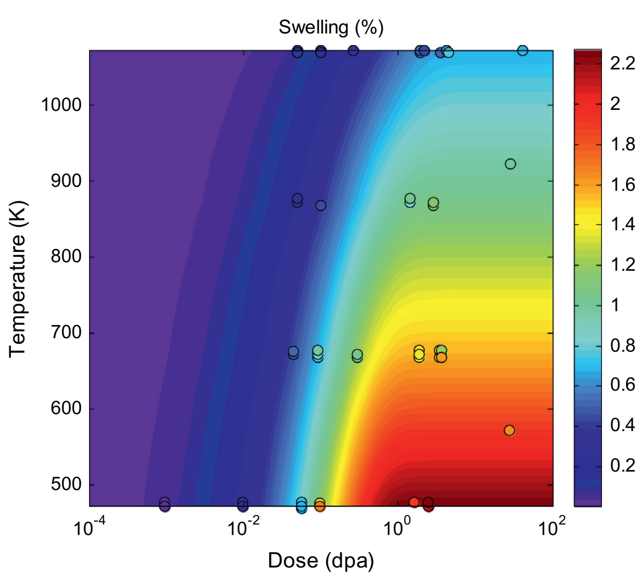

Fig. 1. Contour map of predicted swelling as a function of temperature and dose along with some experimental data points (circles) replotted from [4,22].

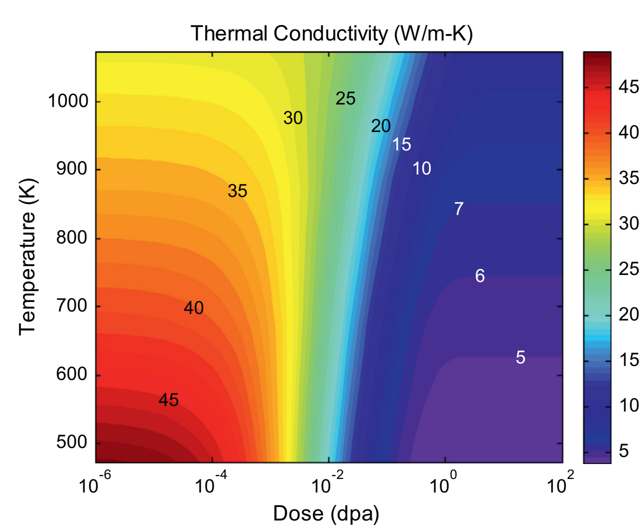

Fig. 2. Contour map of SA3-PyC150A SiC/SiC composite through-thickness thermal conductivity as a function of temperature and dose.

compared to more common variants such as Hi-Nichalon Type-S CVI composite.

2.1.3. Other thermal properties

Other thermal properties that need to be considered are the coefficient of thermal expansion (CTE) and the heat capacity. The effect of irradiation on CTE of SiC/SiC composites is known to be negligible [8]. Accordingly, a baseline temperature-dependent CTE was used from experimental data provided in Ref. [8]. The heat capacity of SiC in the monolithic and the composite form is once again known to be largely independent of irradiation dose. The experimental values that were plugged into the model were extracted from Ref. [4].

2.1.4. Mechanical properties

To provide a complete thermo-mechanical analysis of the SiC/SiC cladding temperature, dose, and the geometrical dependence of mechanical properties of these composite materials must be accurately incorporated into the model. Fortunately these data have become recently available and are included [8]. Consistent with the previous section, the properties for SA3-PyC150A SiC/SiC composite have been chosen to be used during the course of this analysis. As it is the case for monolithic CVD SiC [4], the elastic and shear moduli are expected to decrease slightly as function of temperature. The irradiation effects on E and G can again be correlated to the magnitude of swelling (that represents the extent of defects present in the material), where a slight decrease is also expected. The directional dependence of the elastic and shear moduli, as well as the Poisson's ratio, reported in Ref. [8] is taken into account for the composite material in the unirradiated state. The elastic and shear moduli are then adjusted given only the swelling for the material during the course of model evolution, whereas the value of Poisson's ratio is kept constant (the in-plane Poisson's ratio is assumed to be 0.13 and the through-thickness Poisson's ratio is 0.16).

2.1.5. Creep

Thermal creep for SiC cladding structures is ignored in this analysis since the onset of those processes (>1400 °C) is well above the temperature range pertinent to cladding operation under nominal LWR conditions [25]. However, irradiation creep of SiC, although very limited in magnitude, is active at low temperatures, can play a small role on evolution of the mechanical state of the cladding structure and needs to be taken into account. Recent studies by Katoh et al. [26,27] on CVD SiC correlate the irradiation creep strain rate with the swelling rate with a first-order dependence on the applied stress. This formulation is adopted for the analysis performed here with details on its implementation discussed in the following sections. It is worth noting that irradiation creep and swelling are not fully separate and independent phenomena. In fact, similar to irradiation growth and creep that are coupled in Zr alloys, irradiation creep and isotropic swelling of SiC are also coupled and interdependent. These complex interdependencies are not well understood and are not captured in the framework of the current analysis.

2.1.6. Fission gas release

Fission gas release (FGR) remains an area of active research in the field of nuclear fuel science and engineering and is greatly sensitive to the type and microstructure of the fissile medium as well as the operating regime [28]. In this analysis a very simple yet purposeful FGR model is employed. Essentially it is assumed that the rod internal pressure linearly increases as a function of time from 1 to 20 MPa in 2 years. This very simple assumption was employed to understand the effects of FGR on the mechanical behavior of cladding in a clear manner. Note that the final value of 20 MPa constitutes excessive release and is beyond what is typically seen at end-of-life in LWR fuel pins. However, this value was intentionally set to showcase the effects of rod internal pressure once it surpasses that of coolant pressure.

Table 1
Summary of dose and temperature dependence of material properties for SiC/SiC composite.

Property	Dose dependent	Temperature dependent	References
S	Yes	Yes	[19]
k	Yes	Yes	[8]
α	No	Yes	[4]
C_p	No	Yes	[4]
E, G	Yes	No	[8]
ν	No	No	[8]
E_p, E_r	Yes	No	[8]
ν_p, ν_r	No	No	[8]

2.1.7. Dose- and temperature-dependent properties

Table 1 provides a list of various materials properties used in this model along with whether temperature and dose dependencies for these properties are taken into account using experimental data in the applicable references.

2.2. Solution methodology

The Euler implicit scheme was chosen for the discretization of the heat equation to convert the continuum differential equation into a set of finite-difference or finite-element equations for the 1D and 2D analyses, respectively. As described in the following sections, these equations are in turn assembled in sparse matrices and solved simply given a set of boundary conditions. However, given the complexity presented by temperature- and dose-dependent material properties, in order for the simulation to reflect the entire lifetime of a cladding, a decoupling process similar to that described previously [29] was adopted as a compromise between accuracy and calculation efficiency. The operator splitting algorithm is depicted graphically in Fig. 3. Essentially the spatial variation of material properties is taken into account at each time-step given a first-order extrapolation of those values from the two previous time-steps (Euler implicit method). Given these estimated values, the properties are assumed frozen at the current time-step and the heat equation is then solved. From the new calculated temperature values, the material properties as well as swelling and creep strain rate are updated for each node/element. The final task of the algorithm for each time-step is to carry out the stress calculations. The details and the differences of the analysis method for the 1D and 2D models are described in detail in the following sections.

The initial temperature profile in the fuel (essentially the initial condition for the transient analysis) is calculated in the absence of any irradiation. This is consistent with reactor conditions where thermal equilibrium across the cladding will be reached long before any significant effect of irradiation is experienced within the material. The initial condition is also calculated using the transient equations starting from a uniform temperature distribution and a set of boundary conditions consisting of heat flux from the fuel and convective heat transfer to the coolant. Once the temperature profile equilibrates under these conditions, it is taken as the initial condition and the onset of irradiation. The code takes advantage of an adaptive time mesh to enhance the calculation efficiency. The time-step increases as neutron exposure builds since the accumulation rate of irradiation effects is expected to decrease. The implicit discretization scheme described earlier will provide unconditional L^{∞} stability. This is important in the course of this

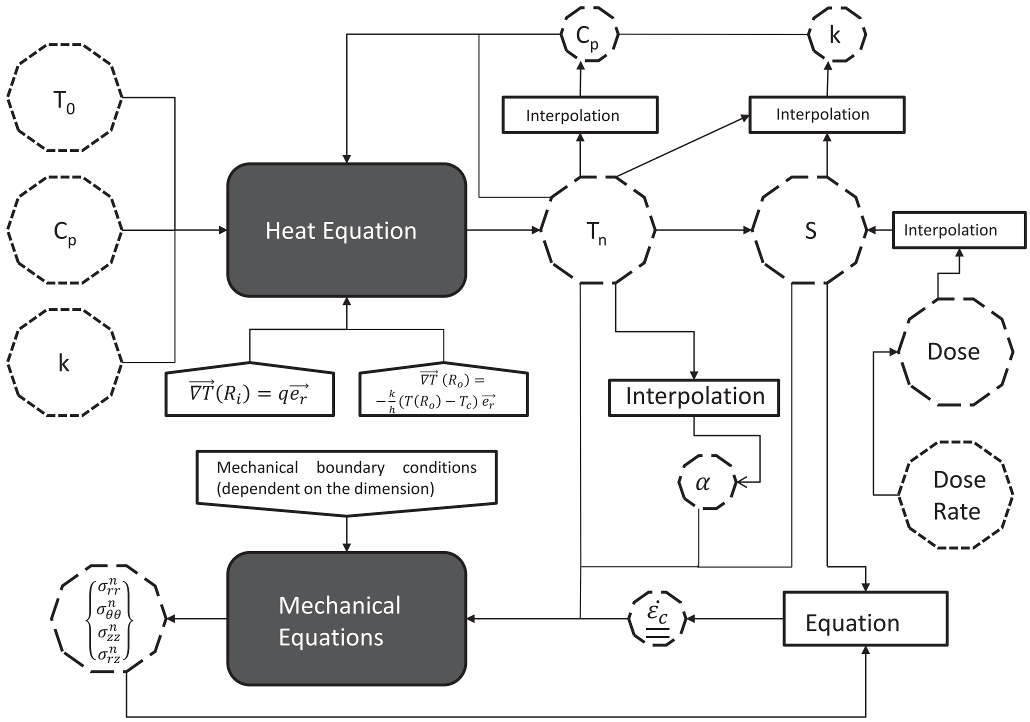

Fig. 3. Algorithm utilized during each time-step.

analysis since an adaptive time mesh is employed and also because of the very fast drop in thermal conductivity at the beginning of the irradiation. However, this comes at the cost of a loss of one order of magnitude in time compared to an optimal Crank–Nicolson [30] semi-implicit scheme (first- vs. second-order accuracy).

2.3. 1-Dimensional finite-difference model

2.3.1. Heat equation

For the 1D analysis, an infinitely long SiC/SiC composite cladding (empty cylinder) without any volumetric heat generation is considered. The cladding is considered to be isotropic, homogeneous, and azimuthally symmetric. Accordingly, all thermal properties that are assumed to be temperature and irradiation dependent (i.e., conductivity, specific heat) are radially and temporally variable, as shown in Fig. 4.

After the thermal equilibrium is reached and the initial condition is established, the cladding experiences a constant dose rate ($\sim 10^{-7}$ dpa/s [31]) and spatially uniform fluence. Since the thermal conductivity varies with neutron dose (see Section 2.1.2), the dose-dependent heat equation is formulated as

$$\frac{\partial}{\partial t}(\rho C_p T) = \frac{1}{r}\frac{\partial}{\partial r}\left(k(D) r \frac{\partial T}{\partial r}\right). \tag{3}$$

Two boundary conditions are imposed on the cladding inner and outer surfaces. The first boundary condition is a heat flux, q, arriving from the fuel pellet to the inner surface of the cladding, as described by Eq. (4). In the 1D analysis, the incoming heat flux is assumed to be constant, axially and azimuthally uniform, and is determined by the linear heat rate (LHR) of the fuel rod. On the outer surface, the convective heat transfer into the coolant sets the boundary condition, as shown by Eq. (5). The heat flux is governed by the difference between the cladding outer surface and the coolant temperatures and the magnitude of the hydraulic heat transfer coefficient. A typical value for the heat transfer coefficient ($10{,}000$ W m^{-2} K^{-1}) is assumed [32]. In the 1D analysis, coolant temperature and the heat transfer coefficient are assumed to be axially and azimuthally uniform and constant at their initial value all along the simulation. These two boundary conditions are realized using two ghost nodes — one on the inner surface and the other on the outer surface.

$$k\overrightarrow{\nabla}T_{(r=r_i)} = -q\vec{e}_r, \tag{4}$$

$$k\overrightarrow{\nabla}T_{(r=r_i)} = -h(T_{r=r_e} - T_c)\vec{e}_r. \tag{5}$$

These boundary relations are assumed to be valid before and all during the irradiation of the material, without any change or dependency on the dose rate and the dose experienced by the cladding. At the onset of the calculation and prior to determining the initial condition before the start of irradiation, a uniform temperature T_c is assumed within the entire cladding.

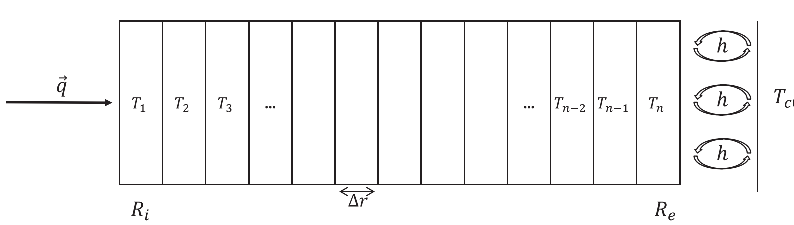

Fig. 4. 1D finite-difference analysis scheme.

2.3.2. Mechanical equations

The cladding geometry in the 1D model remains rotationally symmetrical and axially infinite, while the composite material is assumed to be homogeneous and isotropic. As discussed earlier, Poisson's ratio is independent of temperature and neutron dose, whereas Young's modulus exhibits only dose dependence (therefore, in the following, it is considered as a radially variable property). The two sources of strain in the cladding are both isotropic and arise from thermal expansion, due to the temperature gradient between the outer and the inner surfaces, and from the swelling, which is directly related to the temperature and dose across the cladding thickness. Determination of the magnitude of swelling and thermal expansion coefficient for each radial element is addressed in Sections 2.1.1 and 2.1.3. The swelling strain at each direction equals one-third of the magnitude of the volumetric swelling. This is the case since the swelling phenomenon is isotropic and the resulting strains are small compared to the cladding thickness. Assuming only a small range of deformation is experienced and the material remains in the elastic regime, the constitutive equations (Hooke's Law) are as follows:

$$\varepsilon_r = \frac{1}{E}(\sigma_r - \nu(\sigma_\theta + \sigma_z)) + \alpha(T - T_c) + \frac{S}{3}, \tag{6}$$

$$\varepsilon_\theta = \frac{1}{E}(\sigma_\theta - \nu(\sigma_r + \sigma_z)) + \alpha(T - T_c) + \frac{S}{3}, \tag{7}$$

$$\varepsilon_z = \frac{1}{E}(\sigma_z - \nu(\sigma_\theta + \sigma_r)) + \alpha(T - T_c) + \frac{S}{3}. \tag{8}$$

Generalized plane strain condition was assumed in the axial direction in the 1D analysis. This is a very good assumption for the majority of the cladding height since the cladding thickness is roughly four orders of magnitude smaller than its height. The equilibrium condition and the expression of small deformations in cylindrical coordinates with displacement vectors lead to the following:

$$\frac{d\varepsilon_\theta}{dr} + \frac{\varepsilon_\theta - \varepsilon_r}{r} = 0, \tag{9}$$

$$\frac{1}{r^2}\frac{d}{dr}\left(r^3\frac{d\sigma_r}{dr}\right) = \frac{-E}{1-\nu}\left(\frac{d}{dr}(\alpha T) + \frac{1}{3}\frac{dS}{dr}\right). \tag{10}$$

In order to solve Eq. (10), two boundary conditions are needed that are provided by the assumptions of axially uniform inner and outer pressure (Fig. 5). The inner pressure varies as a function of time as discussed earlier to increase linearly from 1 to 20 MPa at the end of the analysis. The outer pressure is fixed at that of a typical pressurized water reactor (PWR) coolant pressure of 15 MPa.

$$\sigma_{r(r=r_i)} = -P_i \tag{11}$$

$$\sigma_{r(r=r_i)} = -P_e \tag{12}$$

Using the radial equilibrium condition expressed in cylindrical coordinates, the azimuthal stress may be inferred from the radial one by

$$\sigma_\theta = \frac{\partial}{\partial r}(r\sigma_r). \tag{13}$$

The axial stress can then be determined using the Saint Venant's principle. The assumption of no axial load on the top and on the bottom of the cladding is used to determine the axial stress and relies on the fact that in a real reactor the cladding is free to move along the axial dimension (the cladding is not constrained axially, as shown in Fig. 6). This is an immensely important consideration during the course of stress calculations. If one is to incorrectly assume axial constraint, widely different results will emerge that will not be representative of the actual reactor conditions.

The closed pressurized tube with an unconstrained axial condition implies that the mean axial stress is given by

$$\bar{\sigma}_z = \frac{\int_{r_i}^{r_e}\sigma_z(r)rdr}{\int_{r_i}^{r_e}rdr} = \frac{\pi r_i^2(P_i - P_e)}{\pi(r_e^2 - r_i^2)}. \tag{14}$$

Moreover, because the thickness of the cladding is roughly four orders of magnitude smaller than the height, it can also be assumed that the expression of the axial deformation is independent of the radius of the element. These assumptions and the expression of the axial deformation given by Hooke's law, averaged on an axial slice of the cladding, lead to the following derivation:

$$\sigma_z(r) = E(r)\cdot\varepsilon_z + \nu(\sigma_r(r) + \sigma_\theta(r)) - E(r)\cdot\left[\alpha(T(r) - T_c) + \frac{S}{3}\right] - \bar{\sigma}_z \tag{15}$$

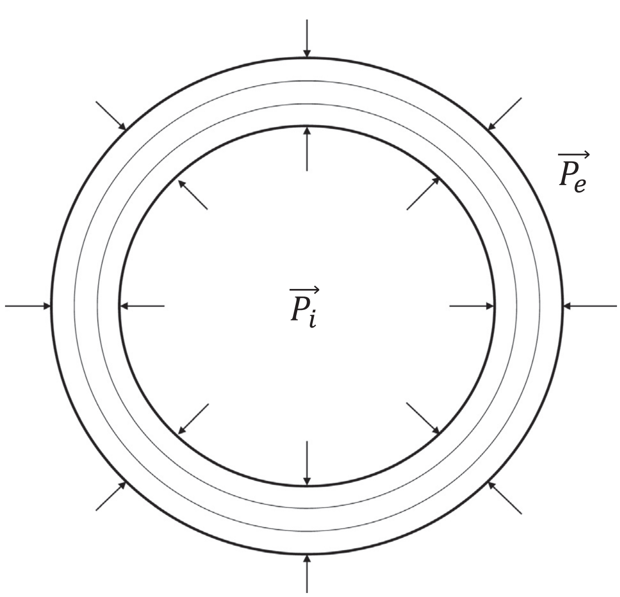

Fig. 5. Representation of the 1D radial stress boundary conditions.

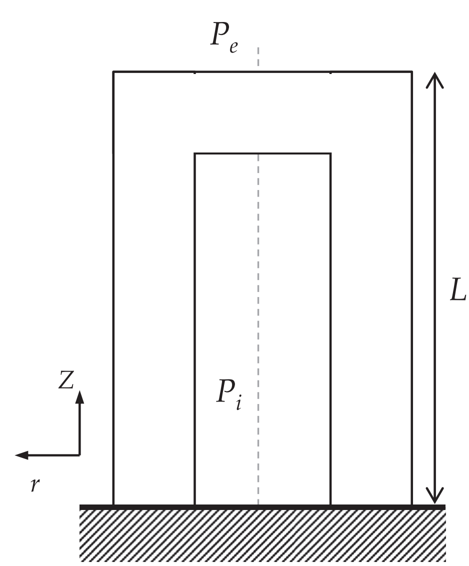

Fig. 6. Representation of the 1D axial boundary conditions.

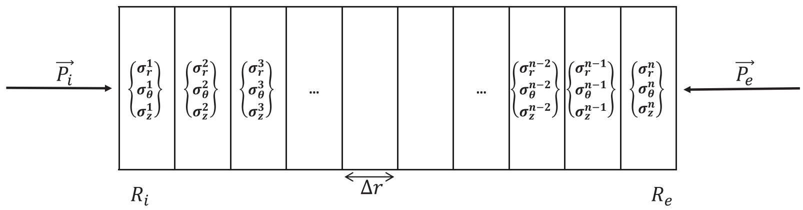

Fig. 7. Cladding mechanical discretization and boundary conditions profile.

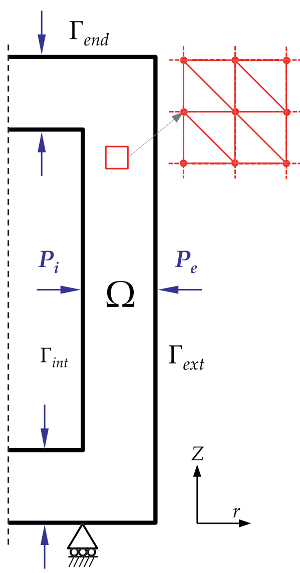

Fig. 8. Spatial domain and load distribution in the 2D finite element model. A depiction of the mesh and node distribution is also shown.

with

$$\varepsilon_z = -\frac{\int_{r_i}^{r_e} \nu(\sigma_r(r) + \sigma_\theta(r))rdr}{\int_{r_i}^{r_e} E(r)rdr} - \frac{\int_{r_i}^{r_e} E(r)\cdot(\alpha(T(r) - T_c) + \frac{S(r)}{3})rdr}{\int_{r_i}^{r_e} E(r)rdr}. \quad (16)$$

Note that the radial dependency of the Young's modulus is taken into account in the previous equations while being ignored during the well-known derivation of Eq. (10). Indeed, if $\frac{\sigma_r \frac{\partial E}{\partial r}}{E^2} \ll \frac{\partial S}{\partial r}$, Eq. (10) is not subject to change. This condition is verified given that $\frac{\partial S}{\partial r} \sim 1\ \mathrm{m}^{-1}$ and $\frac{\sigma_r \frac{\partial E}{\partial r}}{E^2} \sim 10^{-4}\ \mathrm{m}^{-1}$.

Fig. 7 depicts the full discretization scheme for the mechanical analysis.

2.4. 2-Dimensional finite-element model

2.4.1. Methodology

The 2D simulation is designed to solve the axi-symmetrical problem of heat conduction and stress calculation without any azimuthal dependencies. However, unlike the 1D simulation, the axial dependency was taken in account (i.e., a clad of finite length is considered), and so it is necessary to perform the analysis in the radial-axial ($r - Z$) domain. The projection of one of the wall cross sections of the annular cylinder in a $r - Z$ model is simply a rectangle. This domain is designated as Ω, and the boundaries are be designated as Γ_{ext}, Γ_{int}, and Γ_{end}, as shown in Fig. 8.

The heat and stress equations are solved using a finite-element method. Only triangular elements were used to mesh the domain Ω, as shown in Fig. 8, and linear functions (P1) were used to approximate the solution. Linear triangular elements simplify the calculation; however, these elements are subject to volumetric locking for nearly incompressible solid mechanics behavior [33]. Accordingly, this complicates consideration of creep since it constitutes such behavior. Since the magnitude of creep, discussed in Section 2.1.5, is very limited, these complications are overlooked and triangular elements are used. It should be noted that a more cumbersome approach using rectangular elements with second-order interpolation functions would alleviate these complications. Further details on the implementation of the finite-element model and on the mesh are discussed in the Appendix A.

As for the 1D simulation, physical properties are interpolated using experimental data. Each element of the mesh (the triangles) was assumed to have constant physical properties. These properties are determined using the values at the nodes composing the elements. Thus, for an element j, the physical property X_j is obtained by this equation

$$X_j = \frac{\sum x_k}{3}, \quad (17)$$

where x_k are the values at the nodes of the element j. The x_k are calculated using the same extrapolation methodology as the 1D model, and using the value of temperature and fluence (that are assumed uniform) within each element.

2.4.2. Heat conduction equation

Boundary condition As for the 1D model, an azimuthally uniform heat flux was considered at the inner surface of the clad Γ_{int}, and a convective heat transfer with water at the temperature T_c on the outer surface Γ_{ext}. No heat transfer was allowed at the cladding ends. These boundary conditions are summarized in the following equations:

$$k\vec{\nabla} T = -q\vec{e} \quad on\ \Gamma_{int}, \quad (18)$$

$$k\vec{\nabla} T = -h(T - T_c)\vec{e} \quad on\ \Gamma_{ext}, \quad (19)$$

$$\vec{\nabla} = 0 \quad on\ \Gamma_{end}. \quad (20)$$

The 2D model is capable of taking into account axial variations in the incoming heat flux and coolant temperature. Indeed, in a reactor the heat flux is likely to be high at the rod center while coolant temperature rises upward.

Weak formulation To solve the heat equation using the finite-element method, the weak formulation of this equation has to be established as in [34]. The local heat equation is straightforward:

$$\rho C_p \frac{\partial T}{\partial t} = k \triangle T. \quad (21)$$

Consistent with the previously described methodology, an implicit Euler scheme was chosen for temporal discretization, offering an unconditionally stable solution for the L^∞ norm. This leads to this incremental equation:

$$(-kdt\triangle + \rho C_p)T^{n+1} = \rho C_p T^n. \tag{22}$$

Here dt represents the time-step and T^n the temperature at the n^{th} step. After multiplying this equation by a function $v \in H^1(\Omega \times [0;2\Pi])$ and using the integral in the domain $\Omega \times [0;2\Pi]$, one arrives at

$$\int_{\Omega\times[0;2\Pi]} (-kdt\triangle + \rho C_p)T^{n+1}\, v dV = \int_{\Omega\times[0;2\Pi]} \rho C_p T^n\, v dV. \tag{23}$$

Using the Green Theorem, the Von Neumann boundary conditions in Eqs. (18) and (20), and the Robin condition given in Eq. (19), the following result is determined:

$$\begin{aligned}\int_{\Omega\times[0;2\Pi]} k\,dt\,\nabla T^{n+1}\nabla v dV &+ \int_{\Omega\times[0;2\Pi]} \rho C_p T^{n+1}\, v dV\\ = \int_{\Omega\times[0;2\Pi]} \rho C_p T^n\, v dV &+ \int_{\Gamma_{int}\times[0;2\Pi]} dt\, q\, v dS\\ + \int_{\Gamma_{ext}\times[0;2\Pi]} dt\, h\, T_c\, v dS &- \int_{\Gamma_{ext}\times[0;2\Pi]} dt\, h\, T^{n+1}\, v dS.\end{aligned} \tag{24}$$

Then, given azimuthal uniformity for any radial coordinate, r, the boundary value problem reads as follows: Seek $T^{n+1} \in H^1(\Omega)$ such that

$$\begin{aligned}&\int_\Omega k\,dt\,\nabla T^{n+1}\nabla v\, r d\Omega + \int_{\Gamma_{ext}} dt\, h\, T^{n+1}\, v\, r dl + \int_\Omega \rho C_p T^{n+1}\, v\, r d\Omega\\ &= \int_\Omega \rho C_p T^n\, v\, r d\Omega + \int_{\Gamma_{int}} dt\, q\, v\, r dl + \int_{\Gamma_{ext}} dt\, h\, T_c\, v\, r dl, \quad v \in H^1(\Omega).\end{aligned} \tag{25}$$

According to the Lax–Milgram Lemma, a weak solution exists for T^{n+1}. Then using a Galerkin discretization, which is explained in detail in Appendix A, the solution can be approximated as

$$(dtA_1 + B_1)T^{n+1} = dtb_1 + B_1 T^n, \tag{26}$$

where A_1, B_1, and b_1 are two matrices and a vector, as described in Appendix A. The matrix calculations are implemented with Matlab, and the resolution of the linear Eq. (26) takes advantage of the LAPACK library. Sparse matrix descriptions are used appropriately for A and B in order to enhance the calculation efficiency.

2.4.3. Stress equations

Boundary condition As noted earlier, the boundary conditions for the stress calculations are extremely important and can strongly affect the stress profile. The 2D simulation is a good method used for benchmarking the accuracy of the 1D model, in particular the Saint Venant assumption on the axial direction. Otherwise, the stress boundary conditions are exactly the same as the 1D problem:

$$\underline{\underline{\sigma}}.\underline{n} = -P_i \cdot \underline{n} \quad on\ \Gamma_{int}, \tag{27}$$

$$\underline{\underline{\sigma}}.\underline{n} = -P_e \cdot \underline{n} \quad on\ \Gamma_{ext}, \tag{28}$$

$$\underline{\underline{\sigma}}.\underline{n} = -P_e \cdot \underline{n} \quad on\ \Gamma_{end}, \tag{29}$$

where $\underline{\underline{\sigma}}$ is the Cauchy stress tensor and $\underline{n}$ is the normal vector. The cladding is assumed to be entirely free to move. To handle an isostatic problem, and given azimuthal symmetry, the axial displacement of the bottom left-hand corner node follows a Dirichlet condition:

$$u_z(Dirichlet\,Node) = 0. \tag{30}$$

This assumption, as shown in Fig. 8, will essentially just prevent the cladding from translating axially.

Weak formulation The stress problem is considered in small displacement and in small deformation. The displacement vector u is only described by its radial and axial component:

$$u = \begin{pmatrix} u_r \\ u_z \end{pmatrix}. \tag{31}$$

In the cylindrical coordinates, the deformation tensor can be written using Voigt representation:

$$\underline{\underline{\varepsilon}} = \begin{pmatrix} \varepsilon_{rr} \\ \epsilon_{\theta\theta} \\ \varepsilon_{zz} \\ 2\varepsilon_{rz} \end{pmatrix} = \begin{pmatrix} \frac{\partial u_r}{\partial r} \\ \frac{u_r}{r} \\ \frac{\partial u_z}{\partial z} \\ \frac{\partial u_z}{\partial z} + \frac{\partial u_r}{\partial r} \end{pmatrix}. \tag{32}$$

The thermal expansion and the swelling are supposed to be isotropic and may be written as

$$\underline{\underline{\varepsilon}}^T = \alpha(T - T_{c)}\begin{pmatrix} 1 \\ 1 \\ 1 \\ 0 \end{pmatrix}, \quad \underline{\underline{\varepsilon}}^S = \frac{S}{3}\begin{pmatrix} 1 \\ 1 \\ 1 \\ 0 \end{pmatrix}, \tag{33}$$

and consistent with other properties, they are assumed to be constant within each element.

Contrary to the 1D model, the 2D analysis takes into account irradiation creep. For the study, the range of temperature is likely to be between 300 °C and 500 °C and the range of dpa (displacement per atom) between 0 and 10 dpa. According to [27], the creep strain rate is proportional to the swelling rate and the stress via

$$\dot{\varepsilon} = K\dot{S}\sigma. \tag{34}$$

Since creep is a constant volume phenomenon, the flow rules leads to

$$\underline{\underline{\dot{\varepsilon}^c}} = K\dot{S}\underline{\underline{\sigma}}', \tag{35}$$

where $\underline{\underline{\sigma}}'$ is the deviatoric stress tensor,

$$\underline{\underline{\sigma}}' = \underline{\underline{\sigma}} - \frac{1}{3}Tr(\underline{\underline{\sigma}})$$

and K is a theoretically temperature-dependent constant, which is kept constant in the study ($K \simeq 0.55 \times 10^{-10}\ \mathrm{Pa}^{-1}$). Using the implicit methodology, the creep strain, constant within each element, at the time step n is obtained with the creep strain rate of the time step $n-1$:

$$\underline{\underline{\varepsilon^c_n}} = \underline{\underline{\varepsilon^c_{n-1}}} + K(S_n - S_{n-1})\underline{\underline{\sigma_{n-1}}}'. \tag{36}$$

The stress follows the Hooke's law:

$$\underline{\underline{\sigma}} = \underline{\underline{\underline{C}}}(\underline{\underline{\varepsilon}}(u) - \underline{\underline{\varepsilon_0}}), \quad \underline{\underline{\varepsilon_0}} = \underline{\underline{\varepsilon^c_n}} + \underline{\underline{\varepsilon}}^T + \underline{\underline{\varepsilon}}^S. \tag{37}$$

The stiffness tensor $\underline{\underline{\underline{C}}}$ depends on the properties of the specific material. 1D, 2D, and 3D composites have different stiffness tensors. Furthermore, the fabrication process is also important for the mechanical behavior. The code uses by default a 2D composite (Fig. 9) which is wound around the clad. Thus $\underline{\underline{\underline{C}}}^{-1}$ can be explicitly defined by common mechanical properties defined in the nomenclature:

$$\underline{\underline{\underline{C}}}^{-1} = \begin{bmatrix} \frac{1}{E_r} & -\frac{\nu_{pr}}{E_r} & -\frac{\nu_{pr}}{E_r} & 0 \\ -\frac{\nu_{pr}}{E_r} & \frac{1}{E_p} & -\frac{\nu_p}{E_p} & 0 \\ -\frac{\nu_{pr}}{E_r} & -\frac{\nu_p}{E_p} & \frac{1}{E_p} & 0 \\ 0 & 0 & 0 & \frac{1}{G} \end{bmatrix}. \tag{38}$$

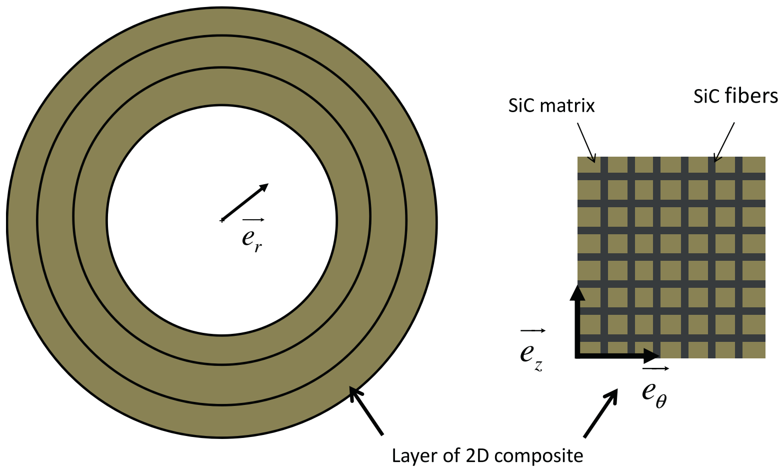

Fig. 9. Design description of a 2D SiC/SiC cladding.

The virtual work principle is then used to build the weak formulation using the $H^1_D(\Omega)$ space [35]:

$$w \in H^1_D(\Omega) := \left\{ w \in H^1(\Omega) | w = 0 \text{ on Dirichlet Node} \right\}. \quad (39)$$

Therefore, the displacement vector is the solution of the following equation: Seek $u \in H^1(\Omega) \times H^1_D(\Omega)$ such that

$$\int_\Omega \underline{\varepsilon}(v) : \underline{\underline{C}}(\underline{\varepsilon}(u) - \underline{\underline{\varepsilon_0}}) r d\Omega = \int_{\Gamma int} P_i(v \cdot \vec{er}) r dl + \int_{\Gamma_{ext}} -P_e(v \cdot \vec{er}) r dl, \quad v \in H^1(\Omega) \times H^1_D(\Omega) \quad (40)$$

According to the Lax–Milgram Theorem and the Korn's inequality, the solution exists. u is also approximated using the Galerkin method:

$$A_2 u = b_2, \quad (41)$$

where A_2 and b_2 are a matrix and a vector, respectively, and are calculated in Appendix A. Similar to the 1D methodology, the sparse matrices in Eq. (41) are calculated using the LAPACK library in Matlab.

3. Results

Results from the 1D and 2D simulations are presented in this section to assess the time-dependent thermo-mechanical behavior of the LWR SiC/SiC composite cladding under irradiation. The reliability of the different simulation strategies is also examined here. Initially, the accuracy of the 1D finite-difference model was benchmarked against the analytical solutions of heat and stress equations given a constant set of physical parameters and its adequacy was confirmed. As will be shown in Section 3.3, the results from the 1D and 2D analyses can be benchmarked against one another without a major discrepancy. This was the case even though completely different analytical strategies were utilized between the finite-difference and finite-element sets of analyses.

For the sake of consistency, the results presented in the following sections are obtained using a set of simplified input parameters presented in Table 2. The study duration is limited to 2 years (as opposed to typical 4.5 years residence lifetime for conventional LWR pins) since early stage phenomena involving evolution and saturation of swelling (occurring at ~1 dpa or 0.3 years) are the important factors under study here. Once swelling saturation occurs, the cladding material properties are no longer subject to change and the only driver for further evolution in thermo-mechanical behavior of the cladding is the rod internal pressure. The simple assumption of linear increase in rod internal pressure provides clear trends while enabling useful observations in the span of this 2-year study. The dose and temperature dependence of the physical properties is taken into account per earlier discussions, as summarized in Table 1.

Table 2
Set of input parameters for the 1D and 2D benchmark analyses.

h	10,000 W/m^2 K
T_c	573.15 K
q (linear heat rate)	350 W/cm
P_i (initial)	1 MPa
P_i (final)	20 MPa
P_e	15 Mpa
r_i	4.18 mm
Dose rate	1×10^{-7} dpa/s
Study duration	6.1×10^7 s ~ 2 years

3.1. 1D simulation results

Fig. 10 shows the results of the 1D analysis that captures the evolution of temperature and various components of stress for different cladding thicknesses as a function of time. Specifically, time evolution of the values at the inner and outer radii is plotted.

The temperature inside the cladding tends to increase due to the drop in thermal conductivity (caused by the irradiation). This phenomenon is more pronounced for the thicker cladding, which presents a larger thermal resistance for heat conduction. Note that Fig. 10 shows the temperature at the outer surface decreasing with an increase in cladding thickness. This is simply due to an increase in the outer surface, which improves the convective heat transfer process given a constant heat transfer coefficient employed in this analysis. Initially, the gradient of temperature across the cladding (governing the differential thermal expansion across the thickness) determines the axial and azimuthal stress profiles. However, as the material experiences irradiation, the swelling strain develops, which significantly alters these stress profiles. Since the magnitude and the rate of swelling decrease with increasing temperature, the cladding experiences larger swelling strains at the outer surface at the onset of irradiation. This will increase the tensile stress components at the inner radius of the cladding. The saturated swelling strain, being roughly an order of magnitude larger than the thermal expansion strains, will induce complete rearrangement of

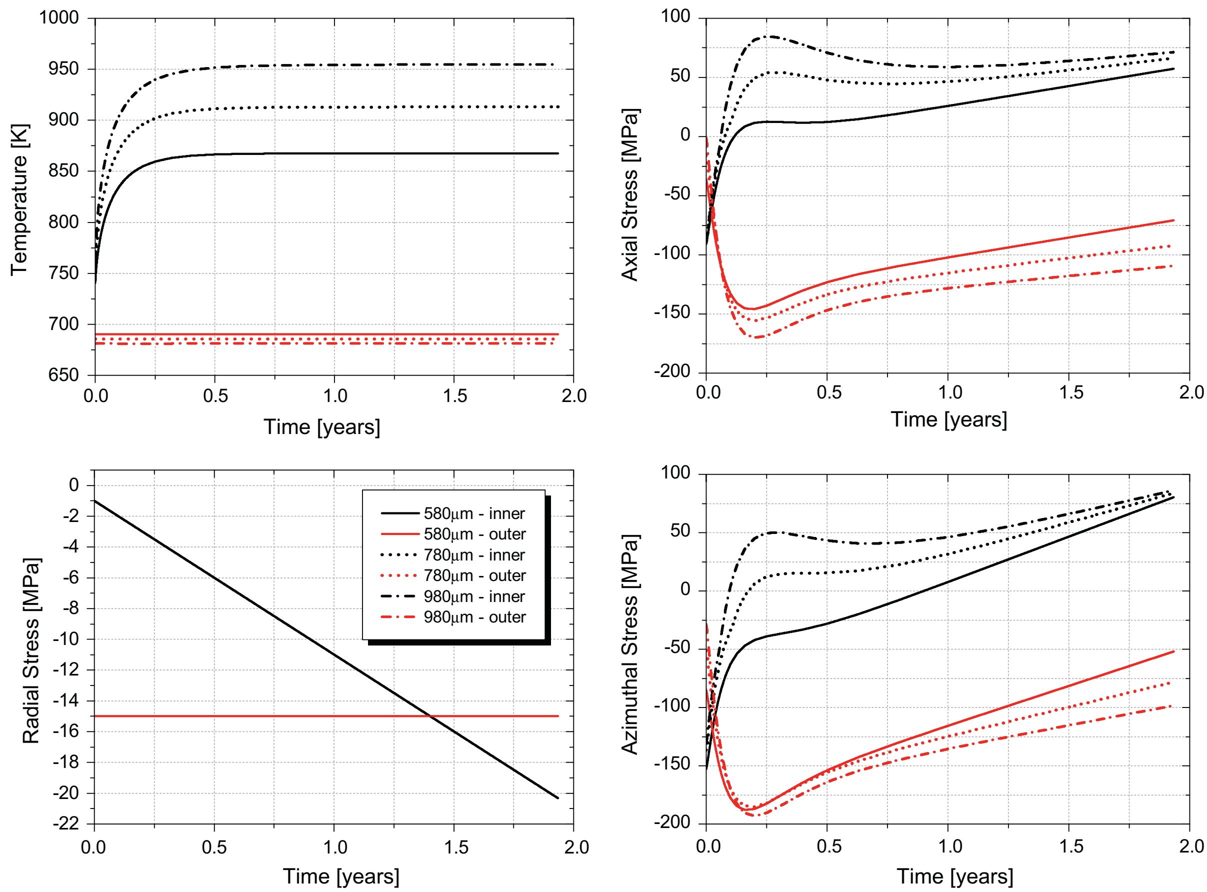

Fig. 10. Time evolution of stress and temperature as a function of time and cladding thickness. Note that r_i is fixed at 4.18 mm.

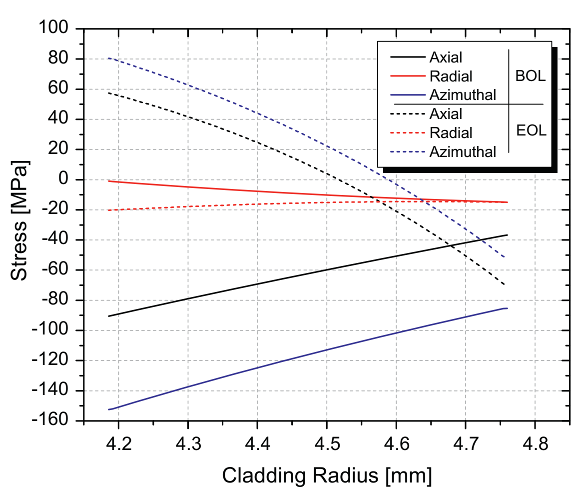

Fig. 11. Stress profiles across the cladding at the beginning (t_0) and at the end of life (t_f). $r_i = 4.18$ mm and $r_e = 4.76$ mm.

the stress profile. Specifically, this results in inversion of axial and azimuthal stress profiles across the thickness, as shown in Fig. 11. The saturation of the swelling results in saturation of material's thermal resistivity, after which the cladding temperature profile does not experience any further change. The axial and azimuthal stress on the other hand will continue to increase due to the fission gas release. Fig. 10 also indicates that the axial and azimuthal tensile stresses tend to increase with an increase in cladding thickness.

At the end of life, the maximum tensile stress is the azimuthal stress on the outermost surface of the cladding. This is partially driven by the increase in the internal gas pressure (20 MPa at the end of the simulation). In fact, without the high internal gas pressure and assuming no fuel-cladding contact, the azimuthal stress would be only compressive for the thin cladding (thickness <0.7 mm) since the coolant exerts hydrostatic pressure on the cladding. Nevertheless, even without excessive fission gas release, a tensile axial stress remains that is largely independent of the pressure differential across the cladding and instead is a function of temperature and swelling gradients across the cladding thickness. Fig. 11 shows the radial, axial, and azimuthal stress profiles across the thickness at the beginning-of-life (BOL) and at the end of a 2-year irradiation period for a 580-µm-thick cladding.

3.2. 2D simulation results

3.2.1. Uniform heat flux and coolant temperature

The results from the 2D finite-element analysis prove consistent with the 1D finite-difference results. Except at the very end of the cladding, the solutions to temperature and stress show no axial dependency, as shown in Fig. 12. This implies that the treatment of the unconstrained axial condition in the 1D analysis is adequate for the 4-m-long cladding. The time evolution of the temperature and stress profiles at the middle of cladding follow the same behavior as the results obtained from the 1D analysis. However, the axial and azimuthal stresses relax at the ends of the cladding, as shown in Fig. 13, since the material is less constrained and has the freedom to elastically deform (essentially approaching plane stress conditions). Another difference is the presence of

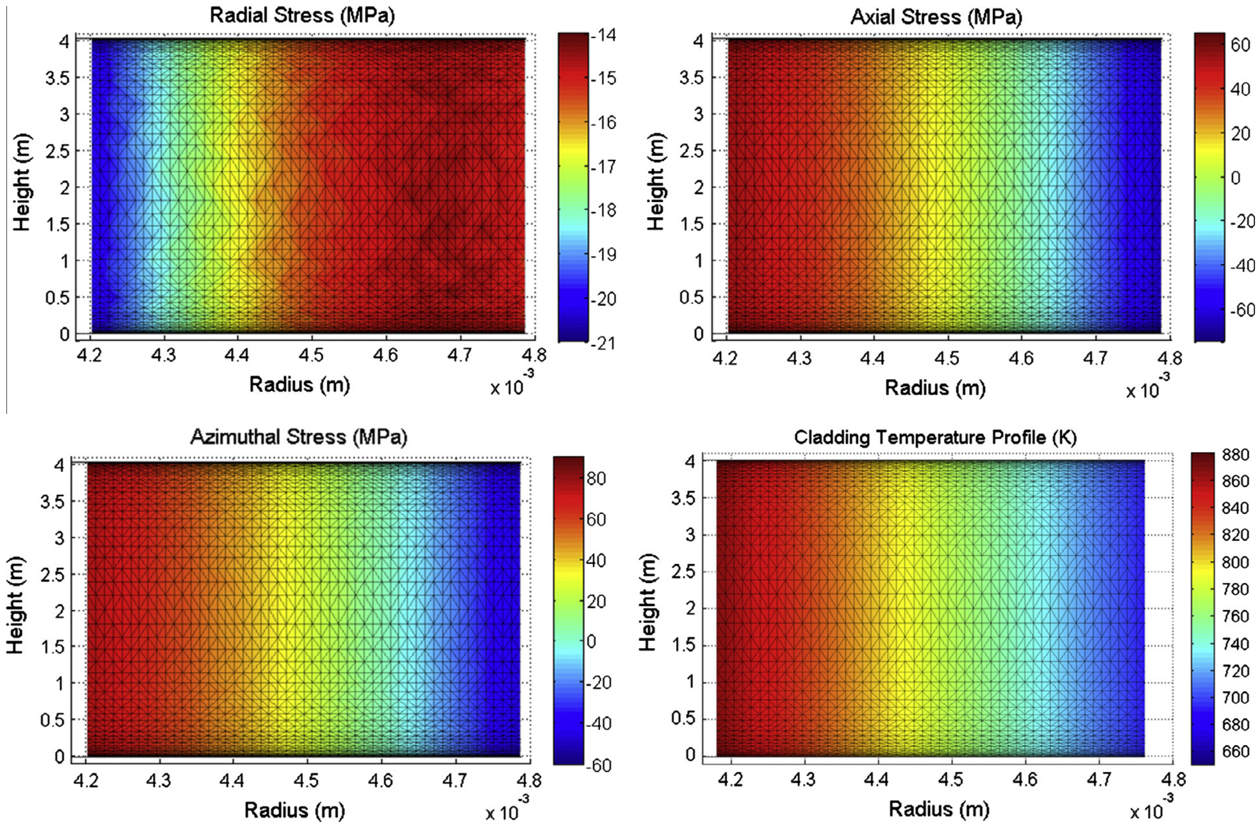

Fig. 12. 2D cat the middle of the cladding and at the end of life (6 dpa). $r_i = 4.18$ mm,$r_e = 4.76$ mm,$L = 4$ m.

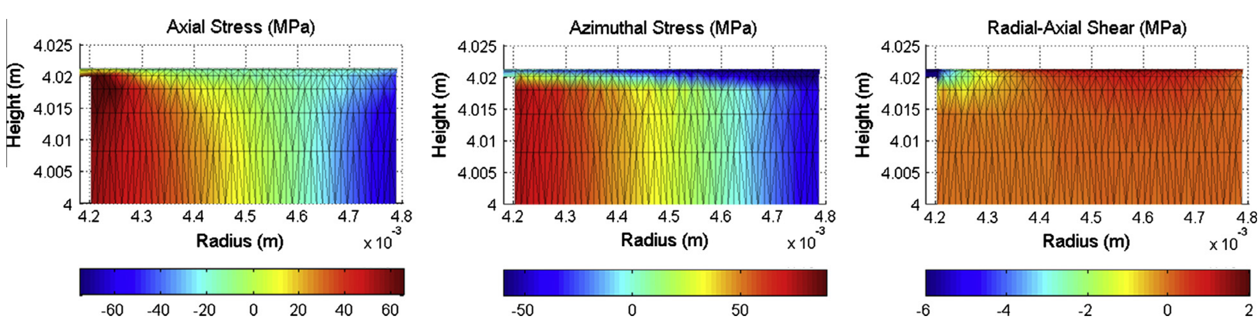

Fig. 13. 2D stress profiles at the end of the cladding and at the end of life (6 dpa). $r_i = 4.18$ mm,$r_e = 4.76$ mm,$L = 4$ m.

shear stress at the end of the cladding (Fig. 13) due to the fact that exterior of cladding expands more than the interior (swelling gradient). Therefore, at the end of the cladding a small axial deformation is observed, as shown in Fig. 14. This deformation (shear deformation) is quite small and leads to small shear stresses.

3.2.2. Variable heat flux and coolant temperature

Another set of simulations were carried out to take advantage of the 2D-finite element method taking into account axial variations in heat flux and coolant temperature profile. The time-dependent heat flux and coolant temperature profiles were from an actual experimental PWR rod irradiated under OSIRIS-R3 experiment [36]. Specifically, the data were from "father" rod K11, and the section was identified as K11-5. Fig. 15 shows the profiles after 1 year of irradiation). The maximum LHR during this test was ~200 W/cm.

Fig. 16 shows the stress profile and temperature profile through the clad after 1 year (~3 dpa). The results of this simulation indicate that nonuniform power and coolant temperature profiles do not significantly alter the behavior of the cladding from that of uniform power and coolant temperature. Despite a change in the temperature (which follows the power and coolant temperature profiles) and in the radial stress (which follows the power profile but remains compressive), the axial and azimuthal stress distributions are similar to the case under which the power profile is uniform.

3.3. Comparison

An important result for consideration is the change in the dimensions of the cladding in the radial and axial directions. Radial displacement, simply calculated using azimuthal strain, is a key parameter both on the inside since it alters the fuel-cladding gap and on the outside since it changes the pitch-to-diameter ratio between the rods. Fig. 17 shows the effects of temperature and swelling, both leading to increased interior and exterior radii. The initial

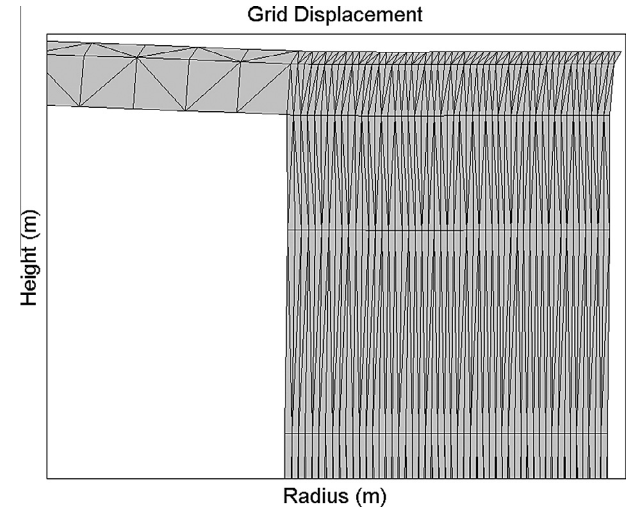

Fig. 14. Depiction of the deformation at the end of the cladding (deformation is magnified).

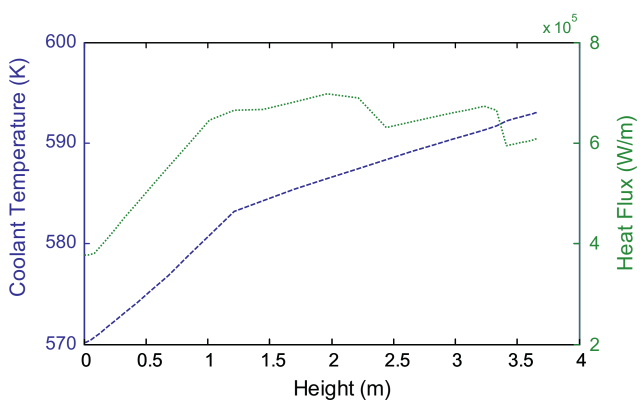

Fig. 15. Heat flux profile and coolant temperature profile after 1 year into the irradiation of K11 rod.

decrease in cladding radius due to the large coolant hydrostatic pressure is small compared to these values. Moreover, the effect of swelling is stronger than the thermal expansion because the outer surface expands more than the inner surface, whereas its temperature is lower. When comparing the finite-difference and finite-element analysis results, the 2D methodology produces a slightly smaller increases in the radii as compared to the case for the 1D method. This is the case since the 2D simulation takes in account the creep phenomenon, which reduces the radius due to outer pressure.

The axial growth, a well-known phenomenon for Zr alloy cladding [37], should also be considered. For the SiC/SiC composite, the axial growth arises mainly from the isotropic swelling. As the saturated volumetric swelling is ~1.5% in this temperature range, axial growth on the order of $\frac{1}{3}$ of that value is expected. The 1D and 2D simulation, in good agreement, reproduce this expectation adequately, as shown in Fig. 18.

Finally, a comparison between the results of stress calculations in 1D and 2D simulations is performed. The absolute error ($\sigma_{2D} - \sigma_{1D}$) is plotted in Fig. 19. 2D and 1D simulations do in fact predict similar stresses, while the absolute error in the azimuthal stress distribution is greater due to the larger absolute values. The main source of this discrepancy arises from neglecting to take into account the creep phenomenon in the 1D model. The maximum relative error is roughly 10%. This figure also shows that the 1D model tends to overestimate the tensile stress. However, since the 1D simulation is much faster than the 2D simulation and more conservative, it appears as the appropriate choice for parametric studies.

4. Discussion

4.1. Pellet-cladding gap

During the course of this analysis, the behavior of the fuel pellet was never considered. Essentially the inner surface of the cladding was never considered to come in contact with the pellet. The applicability of this assumption needs to be verified, and it is clearly a function of initial gap thickness and the swelling rate in the pellet. Pellet-cladding contact in conventional UO_2–Zr alloy clad fuel is a well-recognized phenomenon that takes place at 30–40 MWd/kg UO_2 burnup due to the combined effects of cladding creepdown and fuel pellet thermal expansion and subsequent swelling. In the case of SiC/SiC composite, as reported previously [15,18], the cladding instead swells to expand radially and does not experience any tangible creepdown under the pressure differential across the coolant to the rod internals. Therefore, the evolution in the pellet-cladding gap is the sum of cladding radial expansion and fuel pellet swelling. If one assumes a constant swelling rate on the order of 0.75% per 10 MWd/kg UO_2 burnup for the urania pellet (ignoring initial in-pile densification), the following estimates in gap size evolution as a function of initial gap size (after pellet thermal expansion) and fuel burnup can be made, as shown in Fig. 20.

As indicated in Fig. 20, initially the gap rapidly expands due to swelling of the SiC cladding. As an example this is shown using an arrow for an initial gap thickness of 60 μm that approaches nearly 80 μm at a fuel burnup of approximately 5 MWd/kg UO_2. After the cladding swelling saturates early in life, pellet swelling reduces the gap at a constant rate. For the example case of 60 μm initial gap thickness, the resulting gap at 60 MWd/kg UO_2 fuel burnup is approximately 20 μm. Note that the gap size evolution is remarkably different in the case of SiC cladding when compared to what is expected for Zr alloy cladding. This simple analysis implies that if an initial gap larger than 40 μm is assumed (again, post pellet thermal expansion), the pellet cladding gap never fully closes throughout the fuel lifetime. This result is clearly oversimplified since a constant pellet swelling value is assumed and fuel relocation is ignored. However, the overall trend is indeed applicable to draw a number of general conclusions.

First, pellet-cladding mechanical interaction (PCMI) and fuel behavior under reactivity insertion accidents (RIAs) are expected to be positively influenced. Essentially, lack of or any delay in gap closure will reduce the susceptibility of the cladding to PCMI mode failure under power ramps or RIAs. On the other hand, the second consideration relates to the temperature profile in the pellet that is expected to be adversely affected. An already larger temperature drop across the cladding is now added to a large thermal resistance across the gap that is set to rapidly increase at the early stages of the fuel lifetime. Accordingly, the entire fuel temperature profile is shifted upward, which in turn further reduces fuel thermal conductivity (more Umklapp scattering), affects pellet swelling rate, and results in more fission gas release [15]. These complex effects need to be carefully considered, and a complete analysis is needed to ensure the fuel meets its operational safety envelope [38].

4.2. Failure probability for SiC/SiC composite cladding

The main purpose of this study is to provide a framework for analysis of the thermo-mechanical behavior of SiC/SiC composite cladding for LWR fuel rods. Now that this framework is in place, the stress results determined within the elastic domain can be

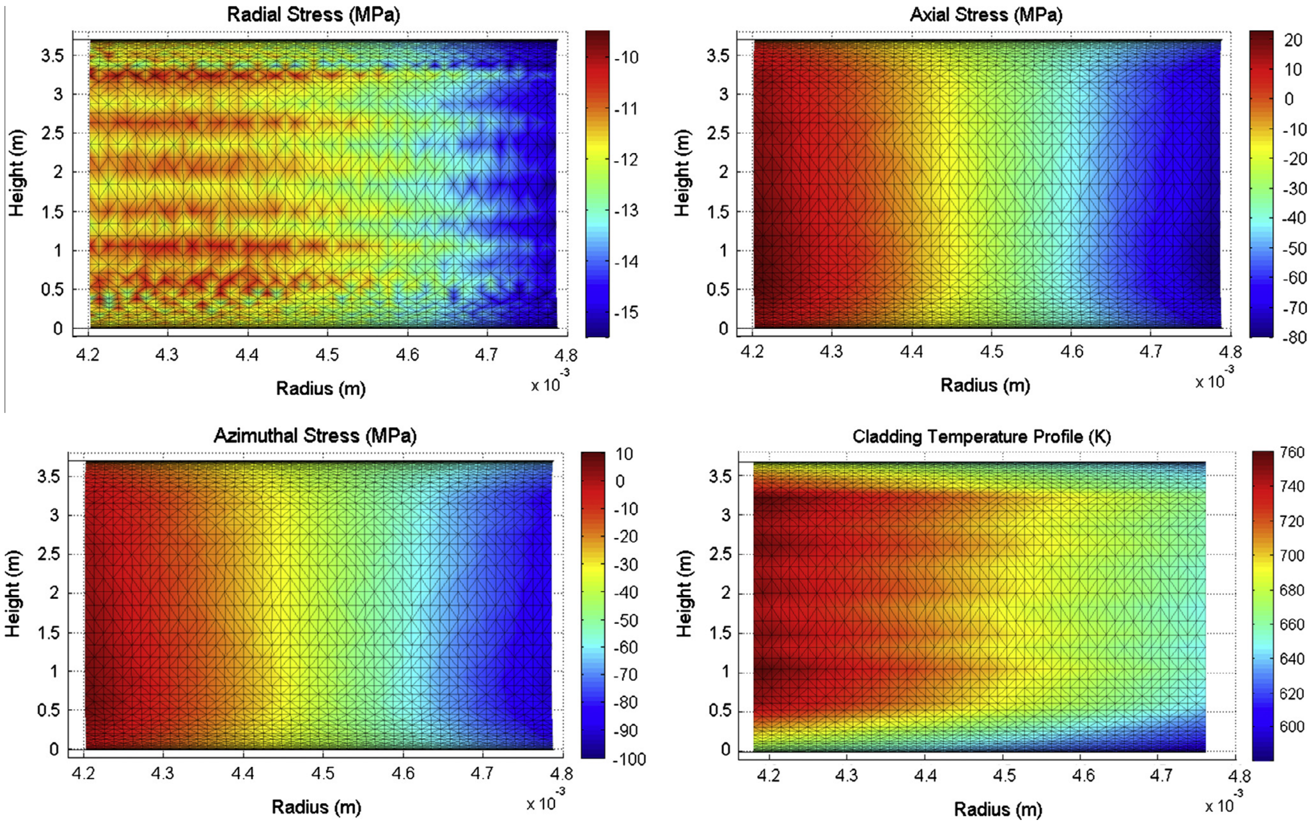

Fig. 16. 2D stress and temperature profiles after 1 year into irradiation of K11 rod using nonuniform power and coolant temperature profiles.

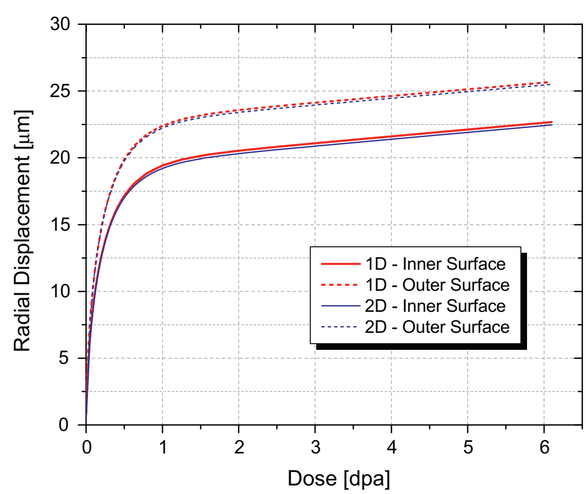

Fig. 17. Radial displacement of the cladding inner and outer radii at the axial mid-plane as a function of neutron dose, $r_i = 4.18$ mm, $r_e = 4.76$ mm.

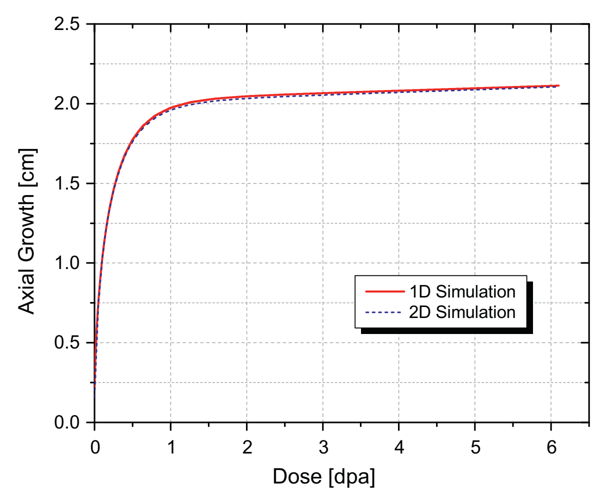

Fig. 18. Axial growth of the element in function of the dose, $r_i = 4.18$ mm, $r_e = 4.76$ mm, $L = 4$ m. The 2D growth is averaged throughout the cladding height.

used to assess the failure probability of the cladding under nominal operating conditions. In contrast to the failure mechanism of metallic cladding, SiC exhibits brittle fracture and therefore a broad distribution in its failure stress. Yet the failure mechanism proves even more complicated for the SiC/SiC composites. As it is explained by Nozawa et al. [39], the matrix of the SiC/SiC composite experiences substantial micro-cracking at a stress of ~70% of the proportional limit stress (PLS) that is reached well below the ultimate tensile strength (UTS). This is the case since the matrix SiC with a higher Young's modulus than that of SiC fiber is the dominant carrier of the load at small strains. Once stresses near the PLS are reached, the matrix cracks (starts to open) and the load is then transferred onto the fibers, which endure it up to UTS. Therefore it is unclear which one of these stress limits (true matrix cracking stress or UTS) constitutes failure for LWR SiC/SiC cladding. It is also noted that, inherent to the processing of the composite, microcracks potentially exist in the as-fabricated state, serving as potential sites for future crack growth. If one considers SiC/SiC composites for structural components within the core, UTS would be an appropriate parameter to set the failure criterion. However, it is likely that interconnected matrix micro-cracking will be

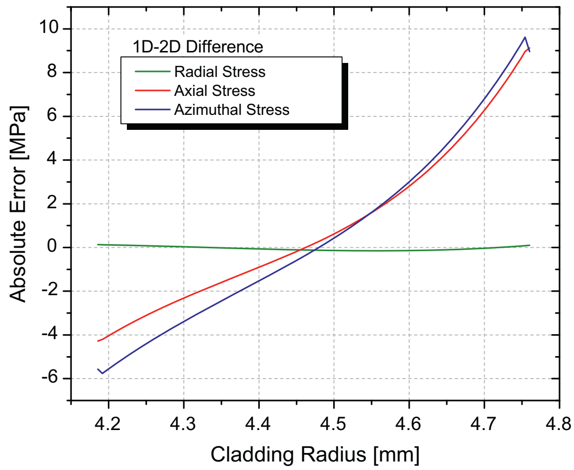

Fig. 19. Absolute error: 2D-1D at the middle of a clad, at the end of life (6 dpa), $r_i = 4.18$ mm,$r_e = 4.76$ mm,$L = 4$ m.

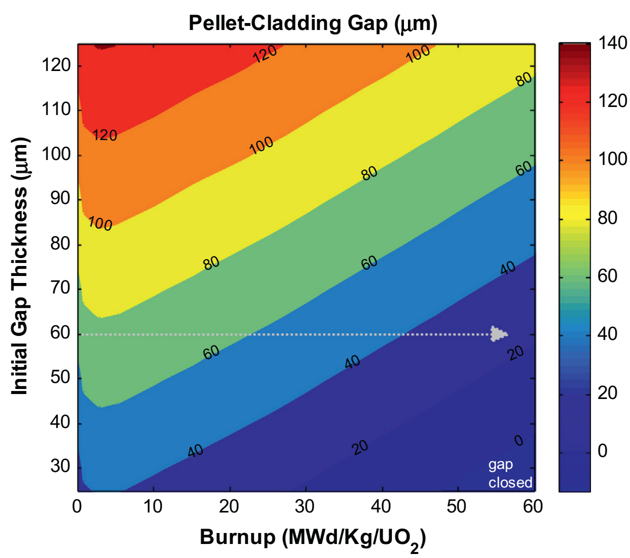

Fig. 20. Pellet-cladding gap size evolution as a function of initial gap size and fuel burnup for SiC/SiC composite cladding. $r_i = 4.18$ mm,$r_e = 4.76$ mm. As an example, the arrow indicates initial expansion followed by contraction of the gap for an initial thickness of 60 μm.

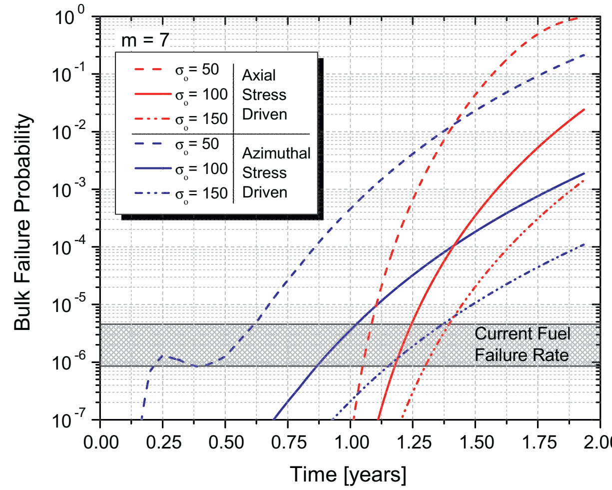

Fig. 21. Bulk instantaneous failure probability due to axial and azimuthal stresses within the cladding. $r_i = 4.18$ mm,$r_e = 4.76$ *mm*.

intolerable for fuel cladding applications where fission product release into the coolant or water ingress into the rod is not allowed. Accordingly, PLS (if not the true matrix cracking stress at ~70% PLS) of the SiC/SiC composite cladding is deemed more appropriate to set the failure criterion for cladding applications.

According to Ref. [8], PLS seems to follow a Weibull distribution (other distribution functions could also prove applicable). Note that in this analysis a two-parameter Weibull is considered. Whether a translated Weibull distribution (three-parameter) is applicable is not known at this point, and such a distribution is not considered in this analysis. The Weibull statistics dictate that the probability of failure initiated from a bulk defect is given by the following equation:

$$P = 1 - exp\left[-\frac{1}{V}\int_{\Omega}\left(\frac{\sigma}{\sigma_0}\right)^m dv\right], \tag{42}$$

where V is the characteristic volume, m is the Weibull modulus (shape parameter), and σ_0 is the characteristic strength (scale parameter). The following result is obtained in a parametric manner with σ_0 varying between 50, 100, and 150 MPa and m kept constant at 7. These values are representative of what is reported by Ref. [8] and can vary across various SiC/SiC composites. Note that normalization against a characteristic volume was not performed since the applicability of this approach for SiC/SiC composites is not likely. It is important to note that the failure probability analysis provided in this paper is simplistic and that a more sophisticated approach considering confidence intervals for Weibull parameters and the volume effect may likely result in further, significantly reduced design allowable stresses.

Fig. 21 shows the instantaneous failure probability as a function of time due to axial and azimuthal stress, separately. Although cumulative failure probability is the relevant parameter for day-to-day operation, the instantaneous probabilities provide insight with regards to critical periods during operation. A band of fuel failure rate probability associated with today's Zr alloy clad LWR pins is also shown in the figure for the sake of comparison [40]. Note that the mechanisms of fuel failure between these two cladding systems are likely to significantly differ.

As expected, the stress-related failures appear later in cladding lifetime triggered by the increasing internal rod pressure due to the assumed FGR. Earlier in life, at least for the thin cladding (~600 μm), the stresses are largely compressive and cannot jeopardize the integrity of the cladding. The onset and magnitude of the increase in axial and azimuthal tensile stresses are quite important and strongly depend on the cladding geometry. As the cladding thickness increases, the larger temperature drop across the cladding results in a steeper swelling gradient. This in turn induces large tensile stresses at the cladding inner surface early in life.

The cladding geometry (essentially inner radius and thickness) plays a major role in cladding integrity during the fuel lifetime. Indeed, it will affect the heat flux at the inner surface at a constant LHR and the temperature distribution within the cladding. As Fig. 22 shows, the failure probability due to axial stress has a strong dependence on thickness and is governed by the swelling gradient across the cladding. Also a slight dependence on the inner radius due to a change in heat flux is noted.

The instantaneous failure probability due to axial stress increases exponentially with thickness and tends to be smaller with a smaller inner radius. The instantaneous failure probability due to azimuthal stress proves more complicated to interpret, as Fig. 23 suggests.

At a constant thickness, as the inner radius increases it tends to increase the failure probability. This is simply explained by the thin

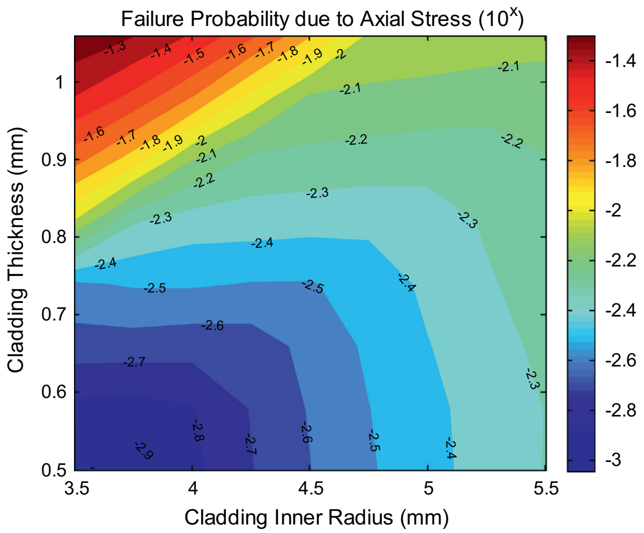

Fig. 22. Contour map of the maximum instantaneous failure probability due to axial stress as a function of cladding geometry.

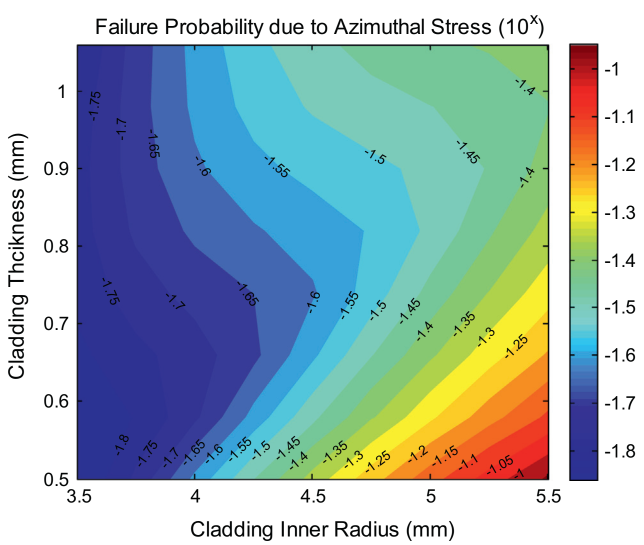

Fig. 23. Contour map of maximum instantaneous failure probability due to azimuthal stress as a function cladding geometry.

tube approximation ($\sigma_\theta = \frac{PR}{\delta}$). The variation in the maximum instantaneous failure probability with thickness shows a minimum around 600–800 μm. While the increase in the thickness will allow the cladding to resist the large internal pressure at the end-of-life (EOL), it will also increase the magnitude of swelling strain, by resulting in higher temperature and therefore swelling gradients. The ~600–800 μm thickness represents a condition where these two effects have reached an optimal balance. Other parameters also affect the failure probability. As shown in Fig. 24, the rod internal pressure at the EOL has a strong effect on the failure probability due to the azimuthal stresses. If the rod internal pressure remains below the coolant pressure, axial stress is the dominant driver for cladding failure. This is in fact what is expected from majority of LWR rods within their lifetime. However, once the internal pressure exceeds the coolant pressure, failure probability due to azimuthal stress becomes important and can exceed that of the axial pressure.

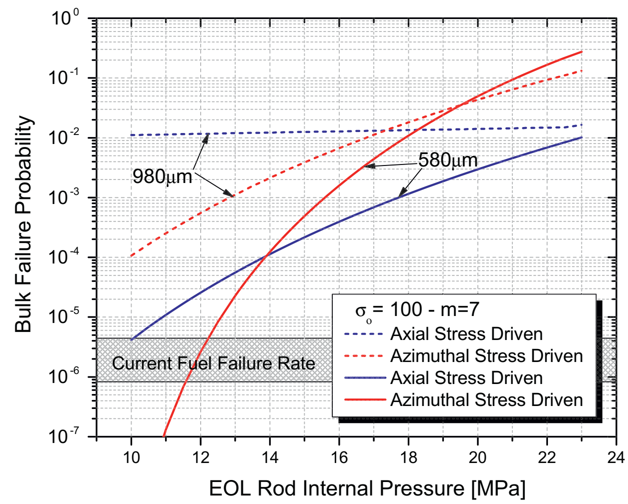

Fig. 24. Azimuthal and axial stress driven failure probabilities as a function of the inner pressure at the end of life for 580 and 980 μm thick cladding, $r_i = 4.18$ mm.

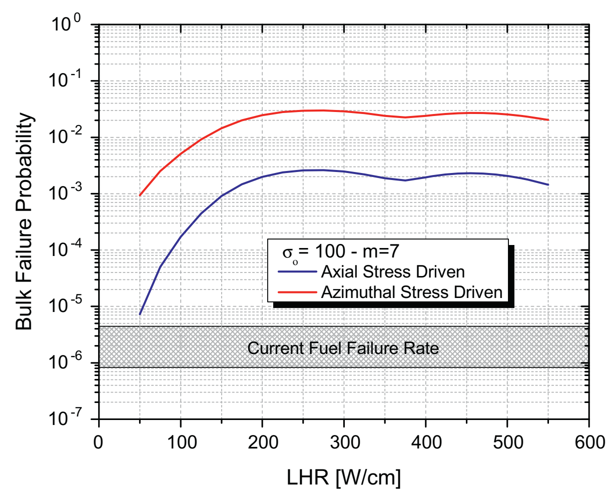

Fig. 25. Maximum instantaneous failure probability due to axial and azimuthal stress as a function of the LHR,$r_i = 4.18$ mm,$r_e = 4.76$ mm.

The linear heat flux arriving from the fuel into the cladding inner surface impacts the axial and azimuthal failure probabilities in a complex manner, as shown in Fig. 25.

On one hand, an increase in the LHR will produce a steeper temperature gradient that in turn increases the swelling gradient and therefore the stress. As noted earlier, this effect will be even more pronounced for more common Type-S fiber SiC/SiC composites that exhibit a significantly lower thermal conductivity than the high-thermal conductivity SA3-PyC150A composite examined in this study. On the other hand, however, a larger LHR will raise the mean temperature across the cladding and decrease the overall magnitude of the swelling and therefore the stress. In mathematical terms one can differentiate Eq. (1) to elaborate further on this point, as shown in Eq. (43).

$$\nabla S \propto b_1 \nabla T e^{b_1 T} \tag{43}$$

Since b_1 is a negative number, it implies that the swelling gradient is opposite and proportional to the temperature gradient. In the meantime, as the mean temperature increases, the exponential term in Eq. (43) drives down the overall magnitude of the swelling gradient. Note that a maximum of failure probability exists at

~400 W/cm for both azimuthal and axial stresses, as shown in Fig. 25.

4.3. Design considerations for SiC/SiC composite cladding

Given the previous set of results and discussions, consideration of the following points are worthwhile toward optimization of the thermo-mechanical behavior of a SiC/SiC composite cladding:

- Maximum of tensile stress is located at the inner surface of the cladding as the fuel lifetime evolves.
- Even for thin claddings (~600 μm), the temperature increase across the thickness proves substantial (even for the high thermal conductivity composite structure considered in this study). For instance, given an LHR of 350 W/cm, the temperature drop across the cladding is in the range of 150–250 °C (for Zr alloy cladding this would be ~40 °C). This will shift up the overall fuel temperature and exacerbate fission gas release.
- An immediate need exists to better understand failure modes and their associated statistical trends (whether related to fission product release or structural damage) for SiC/SiC composites to enable better informed design analyses.
- By ensuring that the internal rod pressure does not exceed the coolant pressure (15 and 7 MPa for PWRs and BWRs, respectively), failure probability due to azimuthal stress for a thin cladding (~600 μm) will be limited in magnitude. If rod internal pressure is set to exceed this value an optimized thickness exists that limits failure probability due to azimuthal stress.
- If the rod internal pressure remains small, the axial failure probability can be limited by choosing a cladding that is less thick (assuming viable fabricability and handling methods exist).
- The inner radius and the rod height are bound to expand and increase under irradiation. Cladding growth of ~2 cm does not appear to be a limiting factor in design. However, the increase in the pellet-cladding gap requires sound consideration to fully grasp the effect on fuel pellet temperature profile and the extent of fission gas release.

5. Conclusions

A multi-module framework for analysis of the in-pile performance of SiC/SiC composite fuel cladding concepts in LWRs has been formulated. The formulation is based on basic equations and is discussed in detail both for the 1D finite-difference and 2D-finite element modules. The analysis framework only considers the cladding and omits any fuel-cladding interaction since radial expansion of the cladding early in life is expected to delay or eliminate the latter. The analysis inputs recent out-of-pile and in-pile materials property data from nuclear-grade SiC/SiC composites to provide a best-estimate analysis. The material property data can be varied across the full spatial extent of the cladding to take into account variable time evolution and directional effects. The 2D module is also capable of inputting axially variable power and coolant temperature profiles to investigate integral performance of a full LWR pin.

This framework is expected to serve as a useful tool during concept design and feasibility studies of SiC/SiC composite cladding concepts and to guide the development activities. Some parametric results are discussed that point to a largely different thermo-mechanical behavior than what one expects in the conventional Zr alloy cladding of LWR fuel pins. This is due to the fundamentally different processes that govern the evolution of these different materials under irradiation. The results of the parametric thermo-mechanical analyses are then coupled with best-estimate Weibull statistics distributions to predict fuel failure probabilities for SiC/SiC composite cladding structures. These probabilistic trends are then used to prescribe basic design guidelines.

Acknowledgments

The aid and technical insight of Joe Rashid and Robert Dunham at Anatech Corp. is gratefully acknowledged. Thorough examination of the manuscript by Alexander Barashev at ORNL is also recognized. The work presented in this paper was partially supported by the Advanced Fuels Campaign of the Fuel Cycle R&D program in the Office of Nuclear Energy, US Department of Energy.

Appendix A

Mesh The 2D-simulation takes advantage of the built-in mesh generator in Matlab. While advanced commercial fuel performance codes such as FALCON [17] use rectangular elements and quadratic interpolation functions, in this analysis the mesh is composed of triangular elements and uses linear interpolation functions. This was done to simplify the code and enhance computational efficiency. Since triangular elements contain only three nodes, the interpolation function and the gradient of this function are easier to estimate. Since the weak formulation of the equations did not involve any second-order term, linear interpolation functions were appropriately and efficiently used.

The meshing scheme for the 2D simulation needs to implemented efficiently in order to optimize for the large aspect ratio of the cladding cross section in the RZ domain. To take into account the large radial gradients in the variables of interest, the radial nodes shall be at least an order of magnitude smaller than the cladding thickness (~ 1 mm). In that case, if a uniform mesh were to be used, given the large length of the cladding (~ 4 m), the mesh would consist of millions of nodes.

Since the axial variations in temperature and stress are expected to be less steep, the mesh can be optimized so that the vertical distance between the axial nodes is relatively large. However, in order to take into account the end effects, the axial variation in the node spacing is set to progressively decrease as one moves away from the mid-plane of the cladding while the radial spacing remains constant. Using this adapted mesh, less than a 1000 nodes are required to simulate a 4-meter-long clad (e.g., 50 radial nodes and 20 axial nodes).

Galerkin method A simple implementation of the Galerkin method is clearly described in related litertaure [34]. However, because of the nonuniform physical properties and because of the specific boundary conditions employed here, the stiffness matrices have to be explicitly defined.

Heat equation The Galerkin method takes advantage of interpolation functions at each node to facilitate a solution to the continuous problem given a discrete and finite set of equations. η_i is the interpolation function at the node *i*. *T*, the solution of the heat equation at each time step, is approximated by $\sum T_i.\eta_i$. Accordingly, the Galerkin method facilitates determination of the vector T^n, given the temperature at each node T_i at the time step *n* by solving Eq. (25). According to Eq. (26), the matrices A_1, B_1, and the vector b_1 are calculated as follows:

$$A_{1,ij} = \sum_{\tau} \int_{\tau} k \cdot r \cdot \nabla\eta_i \cdot \nabla\eta_j^T d\Omega + \sum_{\varsigma_{ext}} \int_{\varsigma_{ext}} h \cdot r \cdot \eta_i \cdot \eta_j dl, \tag{44}$$

$$B_{1,ij} = \sum_{\tau} \int_{\tau} \rho C_p. \cdot r \cdot \eta_i \cdot \eta_j d\Omega, \tag{45}$$

$$b_{1,j} = \sum_{\varsigma_{ext}} \int_{\varsigma_{ext}} q \cdot r \cdot \eta_j dl + \sum_{\varsigma_{int}} \int_{\varsigma_{int}} h. \cdot T \cdot r \cdot \eta_j dl, \tag{46}$$

where τ, ς_{ext}, and ς_{int} designate the triangular elements, the edges composing Γ_{ext}, and the edges composing Γ_{int}, respectively. Considering a given element τ, if the node i or j do not belong to this particular element, one arrives at

$$\int_\tau k \cdot r \cdot \nabla\eta_i \nabla\eta_j^T d\Omega = 0, \tag{47}$$

However, if i and j do belong to τ, k shall then designate the third node and $(r_i, z_i), (r_j, z_j)$, and (r_k, z_k) specify the coordinates of these nodes, respectively. Thus

$$\int_\tau k \cdot r \cdot \nabla\eta_i \cdot \nabla\eta_j^T d\Omega = \frac{k_\tau \bar{r}}{4|\tau|} \begin{pmatrix} z_j - z_k, & r_k - r_j \end{pmatrix} \cdot \begin{pmatrix} z_k - z_i \\ r_i - r_k \end{pmatrix}, \tag{48}$$

where k_τ is the extrapolated thermal conductivity of element $\tau, \bar{r}$ is the medium radius of element τ, and $|\tau|$ is the area of element τ. Using the same routine, if i and j belong to τ, then

$$\int_\tau \rho C_p \cdot r \cdot \eta_i \cdot \eta_j d\Omega = \frac{|\tau| \cdot \rho C_{p,\tau} \cdot \bar{r}}{24} \quad if\ i \neq j, \tag{49}$$

$$\int_\tau \rho C_p \cdot r \cdot \eta_i \cdot \eta_j \cdot d\Omega = \frac{|\tau| \cdot \rho C_{p,\tau} \cdot \bar{r}}{12} \quad if\ i = j. \tag{50}$$

When considering a given edge $\varsigma_{ext.}$, if i and j belong to $\varsigma_{ext.}$, then

$$\int_{\varsigma_{ext}} h \cdot r \cdot \eta_i \cdot \eta_j dl = \frac{h \cdot \bar{r} \cdot |\varsigma_{ext}|}{6} \quad if\ i \neq j, \tag{51}$$

$$\int_{\varsigma_{ext}} h \cdot r \cdot \eta_i \cdot \eta_j dl = \frac{h \cdot \bar{r} \cdot |\varsigma_{ext}|}{3} \quad if\ i = j, \tag{52}$$

and if j belongs to $\varsigma_{ext.}$, then

$$\int_{\varsigma_{ext}} q \cdot r \cdot \eta_j dl = \frac{q_{\varsigma_{ext.}} \cdot \bar{r} \cdot |\varsigma_{ext}|}{2}, \tag{53}$$

where $|\varsigma_{ext}|$ is the length of the edge. In a similar manner

$$\int_{\varsigma_{int}} T_c \cdot r \cdot \eta_j dl = \frac{T_c \cdot \bar{r} \cdot |\varsigma_{int}|}{2}. \tag{54}$$

Stress equation The stress equation is solved essentially using the same method. The same mesh and the same interpolation functions are used. However, the unknown u is not a scalar anymore, but instead it is a vector. To handle this, a vector $U = \sum_1^{2N} u_i \eta_i$ was defined, where N is the number of nodes. If $i \equiv 1\ (2)$, u_i is the radial displacement of the node $\frac{i+1}{2}$; otherwise, it is the axial displacement of the node $\frac{i}{2}$.

The matrices A_2 and the vector b_2 are calculated according to Eq. (41):

$$A_{2,ij} = \sum_\tau \int_\tau \underline{\varepsilon}(\eta_j e_j) : \underline{\underline{C}}(\underline{\varepsilon}(\eta_i \cdot e_i)) r d\Omega \tag{55}$$

$$\begin{aligned} b_{2,j} = &\sum_{\varsigma_{ext}} \int_{\varsigma_{ext}} -P_e \cdot \eta_j (e_j \cdot e_r) r dl + \sum_{\varsigma_{int}} \int_{\varsigma_{int}} P_i \cdot \eta_j (e_j \cdot e_r) r dl \\ &+ \sum_\tau \int_\tau \underline{\varepsilon}(\eta_j \cdot e_j) : \underline{\underline{C}}(\underline{\underline{\varepsilon_0}}) r d\Omega. \end{aligned} \tag{56}$$

If $i \equiv 1\ (2)$,

$$e_i = e_r \tag{57}$$

$$\underline{\varepsilon}(\eta_i \cdot e_i) = \begin{pmatrix} \frac{\partial\eta_i}{\partial r} \\ 0 \\ \frac{\eta_i}{r} \\ \frac{\partial\eta_i}{\partial z} \end{pmatrix}. \tag{58}$$

If $i \equiv 0\ (2)$,

$$e_i = e_z \tag{59}$$

$$\underline{\varepsilon}(\eta_i \cdot e_i) = \begin{pmatrix} 0 \\ \frac{\partial\eta_i}{\partial z} \\ 0 \\ \frac{\partial\eta_i}{\partial r} \end{pmatrix}. \tag{60}$$

As for the heat equation, a given element τ is considered for examination. Six interpolation functions are defined in this domain –– two for each node. If η_i or η_j does not belong to these functions,

$$\int_\tau \underline{\varepsilon}(\eta_j \cdot e_j) : \underline{\underline{C}}(\underline{\varepsilon}(\eta_i \cdot e_i)) r d\Omega = 0. \tag{61}$$

If η_i and η_j do belong to these functions, l, m, and n are assigned as the three nodes and (r_l, z_l), (r_m, z_m), and (r_n, z_n) the coordinates of those nodes such that

$$\int_\tau \underline{\varepsilon}(\eta_j \cdot e_j) : \underline{\underline{C}}(\underline{\varepsilon}(\eta_i \cdot e_i)) r d\Omega = \bar{r} \cdot |\tau| \bar{r} \cdot |\tau| \Phi_j^T \cdot C \cdot \Phi_i, \tag{62}$$

$$\int_\tau \underline{\varepsilon}(\eta_j e_j) : \underline{\underline{C}}(\underline{\underline{\varepsilon_0}}) r d\Omega = \bar{r} \cdot |\tau| \cdot \Phi_j^T \cdot C \cdot \underline{\underline{\bar{\varepsilon}_0}}, \tag{63}$$

$$\underline{\underline{\varepsilon_0}} = \left(\frac{\bar{S}_\tau}{3} + \bar{\alpha}_\tau(\bar{T}_\tau - T_c)\right) \begin{pmatrix} 1 \\ 1 \\ 1 \\ 0 \end{pmatrix} + \underline{\underline{\bar{\varepsilon}^c_{n,\tau}}}, \tag{64}$$

If $i \equiv 1\ (2)$:	If $i \equiv 0\ (2)$:
$\Phi_i = \frac{1}{\lvert\tau\rvert} \begin{pmatrix} z_m - z_n \\ 0 \\ \frac{\lvert\tau\rvert}{3.\bar{r}} \\ r_n - r_m \end{pmatrix} if\ \frac{i+1}{2} = l$	$\Phi_i = \frac{1}{\lvert\tau\rvert} \begin{pmatrix} 0 \\ r_n - r_m \\ 0 \\ z_m - z_n \end{pmatrix} if\ \frac{i}{2} = l$
$\Phi_i = \frac{1}{\lvert\tau\rvert} \begin{pmatrix} z_n - z_l \\ 0 \\ \frac{\lvert\tau\rvert}{3.\bar{r}} \\ r_l - r_n \end{pmatrix} if\ \frac{i+1}{2} = m$	$\Phi_i = \frac{1}{\lvert\tau\rvert} \begin{pmatrix} 0 \\ r_l - r_n \\ 0 \\ z_n - z_l \end{pmatrix} if\ \frac{i}{2} = m$
$\Phi_i = \frac{1}{\lvert\tau\rvert} \begin{pmatrix} z_l - z_m \\ 0 \\ \frac{\lvert\tau\rvert}{3.\bar{r}} \\ r_m - r_l \end{pmatrix} if\ \frac{i+1}{2} = n$	$\Phi_i = \frac{1}{\lvert\tau\rvert} \begin{pmatrix} 0 \\ r_m - r_l \\ 0 \\ z_l - z_m \end{pmatrix} if\ \frac{i}{2} = n$

When considering a given element ς_{int} (or ς_{ext}), four interpolation functions are defined on this edge. If η_j does not belong to these functions or if $j \equiv 0\ (2)$,

$$\int_{\varsigma_{int}} P_i \cdot \eta(e_j \cdot e_r) r dl = 0, \tag{65}$$

$$\int_{\varsigma_{ext}} -P_e \cdot \eta_j (e_j \cdot e_r) r dl = 0. \tag{66}$$

Otherwise,

$$\int_{\varsigma_{int}} P_i \cdot \eta_j (e_j \cdot e_r) r dl = \frac{P_i \cdot |\varsigma_{int}| \cdot \bar{r}}{2}, \tag{67}$$

$$\int_{\varsigma_{ext}} -P_e \cdot \eta_j (e_j \cdot e_r) r dl = \frac{-P_e \cdot |\varsigma_{ext}| \cdot \bar{r}}{2}. \tag{68}$$

References

[1] H. Nickel, H. Nabielek, G. Pott, A. Mehner, Nucl. Eng. Des. 217 (1) (2002) 141–151.
[2] D. Hanson, A Review of Radionuclide Release from HTGR Cores During Normal Operation, EPRI-1009382, Electric Power Research Institute, Palo Alto, CA, 2004.
[3] Y. Katoh, L.L. Snead, C.H. Henager Jr., A. Hasegawa, A. Kohyama, B. Riccardi, H. Hegeman, J. Nucl. Mater. 367 (2007) 659–671.
[4] L.L. Snead, T. Nozawa, Y. Katoh, T.-S. Byun, S. Kondo, D.A. Petti, J. Nucl. Mater. 371 (1) (2007) 329–377.
[5] L. Rovner, G. Hopkins, Nucl. Technol. (United States) 29 (3) (1976).
[6] S. Yajima, J. Hayashi, M. Omori, K. Okamura, Nature 261 (1976) 683–685.
[7] R. Naslain, Compos. Sci. Technol. 64 (2) (2004) 155–170.
[8] Y. Katoh, K. Ozawa, S. Shih, T. Nozawa, R. Shinavski, A. Hasegawa, L. Snead, J. Nucl. Mater. (2013), http://dx.doi.org/10.1016/j.jnucmat.2013.06.040.
[9] K.L. Luthra, Emerging applications and challenges in using ceramics at General Electric, in: Presented at Ceramic Leadership Summit, American Ceramic Society, Baltimore MD August 1–3, 2011.
[10] K. Yueh, K. Edsinger, G. Griffith, J. Garnier, E. Pilat, P. Cantonwine, H. Feinroth, R. Shinavski, Silicon carbide composite for BWR channel application, in: TopFuel 2012, Manchester, UK, September.
[11] K. Yueh, K. Terrani, J. Nucl. Mater. (2013), http://dx.doi.org/10.1016/j.jnucmat.2013.12.004.
[12] H. Feinroth, B. Hao, L. Fehrenbacher, M. Patterson, Progress in Developing an Impermeable, High Temperature Ceramic Composite for Advanced Reactor Clad and Structural Applications, Tech. Rep., American Nuclear Society, 555 North Kensington Avenue, La Grange Park, IL 60526, United States, 2002.
[13] H. Feinroth, et al., A Multi-Layered Ceramic Composite for Impermeable Fuel Cladding for Commercial Water Reactors, Gamma Engineering Report GN-54-03, 2005.
[14] H. Feinroth, M. Ales, E. Barringer, G. Kohse, D. Carpenter, R. Jaramillo, Mechanical strength of CTP Triplex SiC fuel clad tubes after irradiation in MIT research reactor under PWR coolant conditions, in: Ceramic Engineering and Science Proceedings, vol. 30, 2009, p. 47.
[15] D. Carpenter, An Assessment of Silicon Carbide as a Cladding Material for Light Water Reactors. PhD thesis, Massachusetts Institute of Technology, 2010.
[16] G.A. Berna, G. Beyer, K. Davis, D. Lanning, FRAPCON-3: A Computer Code for the Calculation of Steady-State, Thermal-Mechanical Behavior of Oxide Fuel Rods for High Burnup, Tech. Rep., Nuclear Regulatory Commission, Washington, DC, United States. Div. of Systems Technology; Pacific Northwest Lab., Richland, WA, United States, Idaho National Engineering Lab., Idaho Falls, ID, United States, 1997.
[17] Y. Rashid, R. Dunham, R. Montgomery, Fuel analysis and licensing code: FALCON MOD01, Theoretical and Numerical Bases, vol. 1, Tech. Rep., Technical Report ANA-04-0666, EPRI-1011307, Palo Alto, CA, 2004.
[18] Falcon-Based Comparative Assessment of Prototype zr-4 and SiC Fuel Rod, EPRI-1022907, Tech. Rep., Electric Power Research Institute, Palo Alto, CA, 2011.
[19] Y. Katoh, L. Snead, S. Golubov, E. Lara-Curzio, Analyzing irradiation-induced creep of silicon carbide, in: Mechanical Properties and Performance of Engineering Ceramics and Composites III, Wiley, 2007.
[20] Y. Katoh, N. Hashimoto, S. Kondo, L. Snead, A. Kohyama, J. Nucl. Mater. 351 (1) (2006) 228–240.
[21] S. Kondo, Y. Katoh, L.L. Snead, Phys. Rev. B 83 (7) (2011) 075202.
[22] Y. Katoh, T. Nozawa, L.L. Snead, K. Ozawa, H. Tanigawa, J. Nucl. Mater. 417 (1) (2011) 400–405.
[23] P. Klemens, Thermal Conductivity, vol. 1, Academic Press, 1969. p. 1.
[24] L. Snead, S. Zinkle, D. White, J. Nucl. Mater. 340 (2) (2005) 187–202.
[25] C.H. Carter, R. Davis, J. Bentley, J. Am. Ceram. Soc. 67 (11) (1984) 732–740.
[26] Y. Katoh, L.L. Snead, T. Hinoki, S. Kondo, A. Kohyama, J. Nucl. Mater. 367 (2007) 758–763.
[27] Y. Katoh, L.L. Snead, C.M. Parish, T. Hinoki, J. Nucl. Mater. 434 (2013) 141–151.
[28] D.R. Olander, Fundamental Aspects of Nuclear Reactor Fuel Elements, Tech. Rep. TID-26711-P1, Technical Information Center, Springfield, VA, 1976.
[29] K. Terrani, J. Seifried, D. Olander, J. Nucl. Mater. 392 (1) (2009) 192–199.
[30] J. Crank, P. Nicolson, Proc. Camb. Philos. Soc. 43 (1947) 50–64.
[31] H. Heinisch, L. Greenwood, W. Weber, R. Williford, J. Nucl. Mater. 327 (1) (2004) 175–181.
[32] N. Todreas, M. Kazimi, Nuclear Systems I Thermal Hydraulic Fundamentals, Taylor and Francis, 1993.
[33] E. Oñate, J. Rojek, R.L. Taylor, O.C. Zienkiewicz, Int. J. Numer. Methods Eng. 59 (11) (2004) 1473–1500.
[34] J. Alberty, C. Carstensen, S.A. Funken, Numer. Algorithms 20 (2-3) (1999) 117–137.
[35] J. Alberty, C. Carstensen, S.A. Funken, R. Klose, Computing 69 (3) (2002) 239–263.
[36] Quality Assurance Report of Rod FF06E2BV/K11/1090, Rev 2, Tech. Rep., CRACO databse, 1998.
[37] R. Holt, J. Nucl. Mater. 159 (1988) 310–338.
[38] Nuclear Fuel Safety Criteria Technical Review, NEA Report No. 7072, second ed., Tech. Rep., Nuclear Energy Agency, OECD, Paris, 2012.
[39] T. Nozawa, K. Ozawa, H. Tanigawa, Ceram. Mater. Energy Appl. II: Ceram. Eng. Sci. Proc. 577 (2012) 95.
[40] K. Edsinger, EPRI and the zero fuel failures program, Nucl. News 53 (13) (2010) 40.